

Investigating the X-ray enhancements of highly radio-loud quasars at $z > 4$

S. F. Zhu,^{1,2*} W. N. Brandt,^{1,2,3} Jianfeng Wu,⁴ G. P. Garmire,⁵
and B. P. Miller⁶

¹*Department of Astronomy & Astrophysics, The Pennsylvania State University, University Park, PA 16802, USA*

²*Institute for Gravitation and the Cosmos, The Pennsylvania State University, University Park, PA 16802, USA*

³*Department of Physics, 104 Davey Lab, The Pennsylvania State University, University Park, PA 16802, USA*

⁴*Department of Astronomy, Xiamen University, Xiamen, Fujian 361005, China*

⁵*Huntingdon Institute for X-ray Astronomy, LLC, 10677 Franks Road, Huntingdon, PA 16652, USA*

⁶*Department of Chemistry and Physical Sciences, The College of St. Scholastica, Duluth, MN 55811, USA*

Accepted XXX. Received YYY; in original form ZZZ

ABSTRACT

We have investigated the jet-linked X-ray emission from highly radio-loud quasars (HRLQs; $\log R > 2.5$) at high redshift. We studied the X-ray properties of 15 HRLQs at $z > 4$, using new *Chandra* observations for six objects and archival *XMM-Newton* and *Swift* observations for the other nine. We focused on testing the apparent enhancement of jet-linked X-ray emission from HRLQs at $z > 4$. Utilizing an enlarged (24 objects) optically flux-limited sample with complete X-ray coverage, we confirmed that HRLQs at $z > 4$ have enhanced X-ray emission relative to that of HRLQs at $z \approx 1-2$ with matched UV/optical and radio luminosity, at a 4.0–4.6 σ level; the X-ray enhancements are confirmed considering both two-point spectral indices and inspection of broad-band spectral energy distributions. The typical factor of enhancement is revised to $1.9^{+0.5}_{-0.4}$, which is smaller than but consistent with previous results. A fractional IC/CMB model can still explain our results at high redshift, which puts tighter constraints on the fraction of IC/CMB X-rays at lower redshifts, assuming the physical properties of quasar jets do not have a strong redshift dependence. A dominant IC/CMB model is inconsistent with our data.

Key words: quasars: general – X-rays: galaxies – galaxies: high-redshift

1 INTRODUCTION

Quasars (and their parent population of active galactic nuclei, AGNs) are ultimately powered by the accretion process, where gravitational binding energy is released as matter falls into the deep gravitational potential well of the supermassive black hole (SMBH) located in the central region of the host galaxy. The released energy is mainly in the form of quasi-thermal optical/UV photons, likely radiated from an optically thick accretion disk, with a mass-to-radiation conversion efficiency of ~ 0.1 . Accompanying the accretion process, a pair of highly collimated relativistic jets can sometimes launch from the vicinity of the SMBH, perhaps by tapping the spin energy of the SMBH, and extend to galactic and intergalactic scales (e.g. [Begelman et al. 1984](#)). These quasar jets can radiate across the whole electromagnetic spectrum and are most easily detected in the radio band. According

to the flux ratio at rest-frame 5 GHz vs. 4400 Å, i.e. the radio-loudness parameter R ($\equiv f_{5\text{ GHz}}/f_{4400\text{ Å}}$; [Kellermann et al. 1989](#)), the quasar population is divided into radio-quiet quasars (RQQs; $R < 10$) and radio-loud quasars (RLQs; $R > 10$).¹ RLQs are found to be the minority, making up $\sim 10\%$ of the quasar population (e.g. [Ivezić et al. 2004](#)).

X-ray emission is nearly universal from accreting SMBHs ([Brandt & Alexander 2015](#), and references therein). For RQQs, the primary power-law emission in X-rays ($\sim 1-100$ keV) is thought to be created by UV photons from the accretion disk inverse-Compton (IC) scatter-

¹ Use of the terms “radio-loud AGN” and “radio-quiet AGN” is sometimes inappropriate; e.g. when the optical AGN continuum is obscured or when the radio continuum has a strong contribution from non-jet emission (e.g. [Padovani 2017](#)). However, for the powerful type 1 quasars with strong jets under study here, use of this terminology is appropriate (P. Padovani 2018, private communication).

* E-mail: SFZAstro@gmail.com (PSU)

ing off electrons in an optically thin and hot ($\approx 10^9$ K) plasma above the disk, the so-called “accretion-disk corona”. RLQs have an additional jet-linked X-ray component (e.g. Wilkes & Elvis 1987; Worrall et al. 1987), which can outshine the coronal X-ray emission by a factor of ≈ 3 –30 in cases of large radio loudness (e.g. Miller et al. 2011, Miller11 hereafter). This jet-linked X-ray emission is mainly attributed to IC emission of relativistic (non-thermal) electrons that are accelerated by shocks/magnetic reconnection in the jet.

The quasar population has long been known to show strong cosmological evolution in number density (e.g. Schmidt 1968; McGreer et al. 2013; Yang et al. 2016), with RLQs likely evolving differently from RQQs (e.g. Ajello et al. 2009). However, the spectral energy distributions (SEDs) of quasars generally show little evolution to $z > 6$. In X-rays, RQQs at $z > 4$ have similar spectral (e.g. Brandt et al. 2002; Vignali et al. 2003; Shemmer et al. 2006; Nanni et al. 2017) and variability (e.g. Shemmer et al. 2017) properties as those of appropriately matched RQQs at lower redshift, in line with quasar properties in other bands (e.g. Jiang et al. 2006; Fan 2012). Moderately radio-loud quasars ($1 < \log R < 2.5$) at $z > 4$ also have similar X-ray properties to their low-redshift counterparts (e.g. Bassett et al. 2004; Lopez et al. 2006; Saez et al. 2011), while the highly radio-loud quasars (HRLQs; $\log R > 2.5$) show an apparent enhancement in the X-ray band at high redshift (Wu et al. 2013, Wu13 hereafter).

These X-ray studies of high- z RLQs are inconsistent with one of the leading models for quasar jets based on X-ray photometric imaging of low- z objects, where the IC process involving cosmic microwave background (CMB) photons is thought to play an important role. CMB photons have long been proposed to be seeds for the IC process that can effectively produce X-rays (e.g. Felten & Morrison 1966; Harris & Grindlay 1979; Feigelson et al. 1995). One relevant case is quasar lobes (e.g. Brunetti et al. 1999), where relativistic electrons are coupled with CMB photons and produce X-ray emission. After the discovery of the X-ray jet of PKS 0637–752 (Chartas et al. 2000; Schwartz et al. 2000) by *Chandra*, the application of the IC/CMB mechanism to kpc-scale quasar jets become popular. The X-ray jet of PKS 0637–752 is so luminous (relative to the optical) that it cannot be readily produced by other mechanisms (e.g. Schwartz et al. 2000; Harris & Krawczynski 2002), while a modern version of the IC/CMB model can explain radio-to-X-ray SEDs of individual jet knots and maintains the assumption of equipartition. This modern version of the IC/CMB model has two essential requirements: that the kpc-scale quasar jets are relativistic with bulk Lorentz factor ~ 10 and are observed at small angles to our line of sight (Tavecchio et al. 2000; Celotti et al. 2001). These two ingredients naturally explain the one-sidedness of many X-ray jets that are commonly detected in surveys of low- z quasar jets (e.g. Sambruna et al. 2004; Marshall et al. 2005; Kataoka & Stawarz 2005).

In spite of the apparent initial success of the (beamed) IC/CMB model in low- z objects, X-ray studies of high- z RLQs provide a critical piece of evidence against using this model to explain the dominant majority of the X-ray emission from quasar jets. The CMB energy density has a strong cosmological evolution ($U_{\text{CMB}} \propto (1+z)^4$), which is

not reproduced in the jet-linked X-rays from RLQs. The X-ray luminosities of the few resolved jets at high redshift are usually only a few percent that of the cores (similar to large-scale jets at low redshift; e.g. Siemiginowska et al. 2003; Yuan et al. 2003; Saez et al. 2011; Cheung et al. 2012; McKeough et al. 2016), and useful X-ray upper limits on extended jet emission exist for many more RLQs (e.g. Bassett et al. 2004; Lopez et al. 2006; Wu13). Additionally, the jet-linked core emission (which could include X-ray emission from foreshortened kpc-scale jets in some systems) at high redshift does not show the dramatic enhancement predicted by the IC/CMB model (e.g. Bassett et al. 2004; Lopez et al. 2006; Miller11; Wu13). Furthermore, there are other multiple lines of evidence against the most-straightforward IC/CMB model: the tension between the observed and predicted relative brightness distribution in the X-ray and radio bands, the excessive requirement for the jet power, the need for extremely small viewing angles, the high polarisation of the optical emission from some jet knots suggestive of synchrotron emission, and the non-detections of γ -ray emission from quasar jets (e.g. Harris & Krawczynski 2006; Uchiyama et al. 2006; Meyer & Georganopoulos 2014). Alternative models for the luminous low- z X-ray jets often involve an *ad hoc* high-energy synchrotron component (e.g. Atoyan & Dermer 2004).

Even if the IC/CMB process does not play a dominant role, we should expect some IC/CMB X-ray emission from AGN jets; the question is the level of contribution from this process (e.g. Harris & Krawczynski 2006), which could be revealed by studying high-redshift radio-luminous quasars in X-rays. HRLQs rank as the top 5% of the RLQ population in radio loudness (see Fig. 1), and HRLQs at $z > 4$ harbour the most-powerful relativistic jets from the first SMBHs in the early universe, when the CMB photon field is > 625 times more intense than now. Wu13 compared the X-ray emission of a sample of HRLQs at $z > 4$ (median $z = 4.4$) with that of another sample of HRLQs at $z < 4$ (median $z = 1.3$) with matched UV/optical and radio luminosity, and found an X-ray enhancement for the HRLQs at $z > 4$ at a 3 – 4σ level. HRLQs at $z > 4$ have stronger X-ray emission than their counterparts at $z < 4$, by a factor of ≈ 3 on average. There is also evidence for a 5σ X-ray enhancement in another independent sample of HRLQs at $z = 3$ – 4 that is drawn from Miller11.

To explain the redshift dependence of the relative X-ray enhancement of HRLQs, Wu13 proposed a *fractional* IC/CMB model, in which CMB photons are relevant only on the scale of ~ 1 – 5 kpc, with photons from the central engine dominating at smaller distance (e.g. Ghisellini & Tavecchio 2009). At scales beyond a few kpc, the jet has already decelerated so that CMB photons in the rest frame of the jet are not intense enough for the IC/CMB mechanism to be significant (e.g. Mullin & Hardcastle 2009; Meyer et al. 2016; Marshall et al. 2018). The cosmologically evolving IC/CMB X-ray emission only contributes a fraction of the overall X-ray emission from HRLQs with the rest coming from (redshift-independent) IC processes on small scales that involve seed photons from the central engine. The fraction was estimated to be $\approx 6\%$ at $z \approx 1.3$ by Wu13 and rises with redshift. Alternatively, the results of Wu13 can also be explained by a scenario where the star-forming activity of the hosts provides infrared/optical photons that are

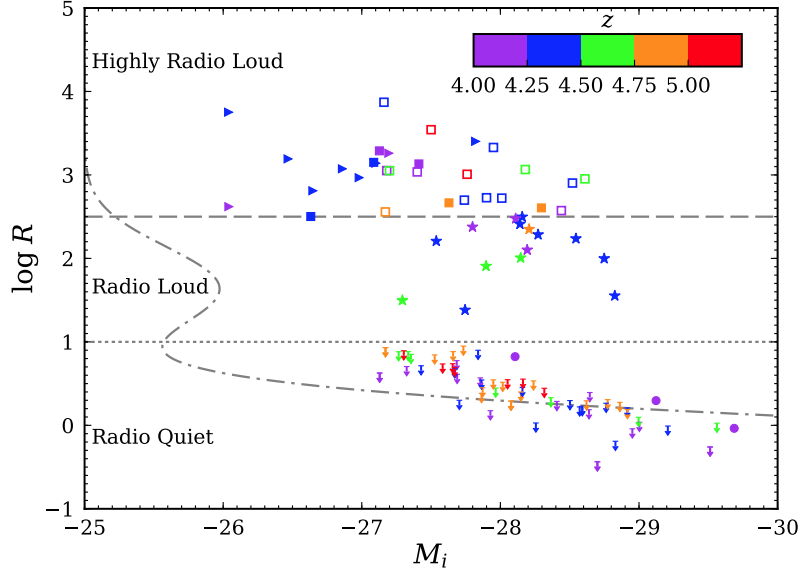


Figure 1. The distribution of $z > 4$ HRLQs in the $\log R - M_i$ plane, compared to moderately radio-loud quasars and RQQs at $z > 4$. The filled squares and triangles are the *Chandra* Cycle 17 objects and archival data objects, respectively. The open squares are the HRLQs of Wu13. The filled stars are moderately radio-loud quasars at $z > 4$ (Bassett et al. 2004; Lopez et al. 2006; Miller11). The filled circles and downward arrows represent the radio-quiet SDSS quasars at $z > 4$ that have sensitive X-ray coverage. All the symbols are color-coded based on their redshifts using the color bar at the top right of the figure. The dotted and dashed lines indicate our criteria for RLQs and HRLQs. The dash-dotted curve (with an arbitrary linear scale) shows the radio-loudness distribution of SDSS quasars (Ivezić et al. 2004), which shows that HRLQs reside in the tail of high radio-loudness.

IC scattered into the X-ray band. This scenario requires the host galaxies of high-redshift quasars to have enhanced star-formation activity (e.g. Wang et al. 2011; Mor et al. 2012; Netzer et al. 2014). In this case, the IC/CMB process becomes even less relevant.

The sample of 17 HRLQs at $z > 4$ used in Wu13 suffers from heterogeneity and limited size, which renders their $\approx 4\sigma$ results only suggestive. Here, we aim at confirming the X-ray enhancement of HRLQs using a larger and more uniformly selected sample. We obtained new *Chandra* observations for 6 HRLQs at $z > 4$ and present their X-ray properties in the paper. We also present X-ray properties of another nine HRLQs at $z > 4$ that have archival *Swift* or *XMM-Newton* data. We describe our sample selection in Section 2, and X-ray data analyses in Section 3. In the following sections, we adopt a flat Λ CDM cosmology, with $H_0 = 70.0 \text{ km s}^{-1} \text{ Mpc}^{-1}$ and $\Omega_m = 0.3$ (e.g. Planck Collaboration et al. 2016).

2 SAMPLE SELECTION

We started with a primary sample that was selected by Wu13 from the SDSS quasar catalog Data Release 7 (DR7; covering 9380 deg^2 of sky area; Schneider et al. 2010) and NED.² They have utilized the 1.4 GHz NRAO VLA Sky Survey (NVSS; Condon et al. 1998), which has provided homogeneous radio coverage for the full sky area of $\approx 34,000 \text{ deg}^2$ north of $\delta = -40^\circ$. For high- z RLQs identified in current wide-field optical/UV surveys (i.e. $m_i \lesssim 21$), if an object satisfies the HRLQ criterion of $\log R > 2.5$, it should have been

² <https://ned.ipac.caltech.edu/>

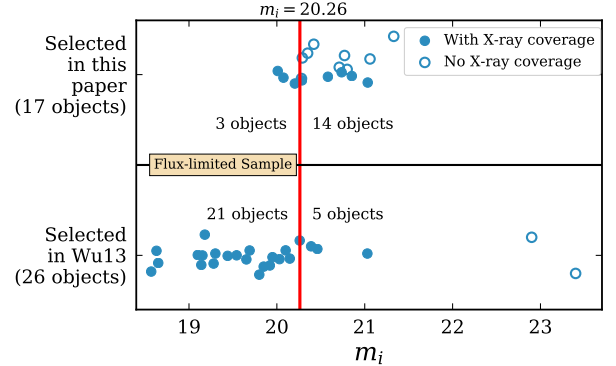


Figure 2. The m_i of the 43 HRLQs that were selected in this paper (17 objects) and in Wu13 (26 objects). The blue solid circle are the objects with sensitive X-ray coverage, while blue open circles are the objects without sensitive X-ray coverage. The vertical red line marks the magnitude cut for the flux-limited sample. Object locations along the vertical axis are only used to distinguish between the objects selected by Wu13 and in this paper. Additionally, each data point is also randomly perturbed in the vertical direction to avoid overlapping.

detected by the NVSS given its sensitivity ($\approx 2.5 \text{ mJy}$).³ Among the resulting sample of 26 HRLQs,⁴ 17 with sensitive X-ray coverage (typically reaching $F_X \approx 10^{-14} \text{ erg cm}^{-2}$

³ We hereafter refer to objects at $z > 4$ as high-redshift/high- z objects and objects at $z < 4$ as low-redshift/low- z objects.

⁴ SDSS J003126.79+150739.5 and SDSS J123142.17+381658.9 are in Table 2 of Wu13. However, they do not satisfy the criterion of $\log R > 2.5$ if we take their rest-frame 2500 \AA luminosities from

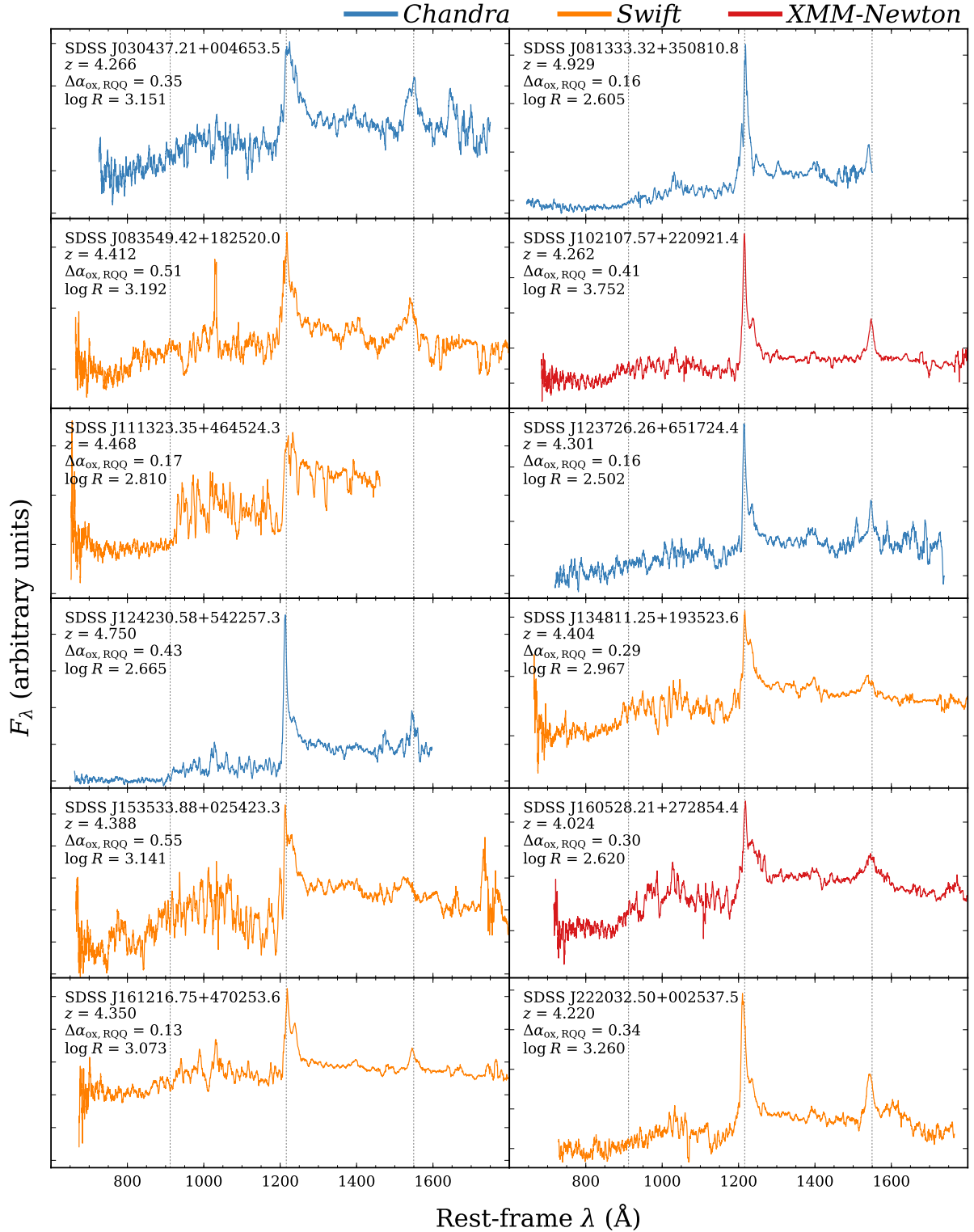


Figure 3. The rest-frame UV spectra of the HRLQs that are in the SDSS quasar catalogs, ordered by RA. The object name, redshift (z), $\Delta\alpha_{\text{ox,RQQ}}$ (the difference between the measured value of α_{ox} and the expected $\alpha_{\text{ox,RQQ}}$, see the description of Column 16 in Section 3.5), and radio-loudness parameter ($\log R$) are shown in the top-left corner in each panel. The spectra do not show strong dependence on $\Delta\alpha_{\text{ox,RQQ}}$, z , or $\log R$. We have plotted the spectra with different colors according to their X-ray data as labeled, where the *Chandra* Cycle 17 objects are blue. The y-axis is in linear scale with arbitrary units. Each spectrum has been smoothed using a 21-pixel boxcar filter. Two emission lines (Ly α $\lambda 1216$ and C IV $\lambda 1549$) and the Lyman limit have been labeled with the dotted vertical lines. Similar spectra can be found in Fig. 3 of Wu13 for the Wu13 objects.

Table 1. X-ray observation log.

Object Name	R.A. (deg)	Dec. (deg)	Instr.	z^a	Obs. Date	Obs. ID ^b	Exp. Time ^c (ks)	FL ^d	Ref. ^e
<i>Chandra</i> Cycle 17 Objects									
SDSS J003126.79+150739.5	7.8617	15.1277	ACIS-S	4.296	2016/06/09	18442	5.4	N	-
B3 0254+434	44.4962	43.6438	ACIS-S	4.067	2015/12/12	18449	5.5	Y	1
SDSS J030437.21+004653.5	46.1551	0.7816	ACIS-S	4.266	2015/11/28	18443	5.9	Y	-
SDSS J081333.32+350810.8	123.3889	35.1363	ACIS-S	4.929	2015/12/19	18444	6.0	Y	-
SDSS J123142.17+381658.9	187.9257	38.2830	ACIS-S	4.115	2016/02/13	18445	6.0	N	-
SDSS J123726.26+651724.4	189.3594	65.2901	ACIS-S	4.301	2016/08/21	18446	7.9	N	-
SDSS J124230.58+542257.3	190.6274	54.3826	ACIS-S	4.750	2016/05/16	18447	4.9	Y	-
PMN J2314+0201	348.7030	2.0309	ACIS-S	4.110	2016/01/15	18448	5.9	Y	2
Archival Data Objects									
SDSS J083549.42+182520.0	128.9559	18.4222	XRT	4.412	2017/01/10 – 2017/05/25	00087221001	45.8	N	-
SDSS J102107.57+220921.4	155.2816	22.1560	EPIC-pn	4.262	2008/05/30	0406540401	8.1	N	-
SDSS J111323.35+464524.3	168.3473	46.7568	XRT	4.468	2016/07/05 – 2016/07/20	00703176000	52.9	N	-
SDSS J134811.25+193523.6	207.0469	19.5899	XRT	4.404	2017/11/29 – 2018/01/15	00087542001	46.6	Y	-
SDSS J153533.88+025423.3	233.8912	2.9065	XRT	4.388	2017/01/06 – 2017/01/26	00087222001	26.4	Y	-
SDSS J160528.21+272854.4	241.3675	27.4818	EPIC-pn	4.024	2011/05/01	0655571401	11.0	N	-
SDSS J161216.75+470253.6	243.0698	47.0482	XRT	4.350	2017/11/08 – 2017/12/13	00088204001	48.7	N	-
PMN J2134–0419	323.5501	–4.3194	XRT	4.346	2013/06/16 – 2013/06/20	00032624001	25.1	Y	2
SDSS J222032.50+002537.5	335.1354	0.4271	XRT	4.220	2013/07/01 – 2013/08/29	00032626001	43.5	Y	-

^a Redshifts for objects in the SDSS DR7 quasar catalog and the SDSS DR14 quasar catalog are from Hewett & Wild (2010) and Páris et al. (2018), respectively. Redshifts for other objects are from NED.

^b We merged multiple observations of the same target for archival *Swift*/XRT data, while only the first observation is listed in the table. The full observation IDs are 00087221001–00087221023 for SDSS J083549.42+182520.0, 00703176000–00703176011 for SDSS J111323.35+464524.3, 00087542001–00087542016 for SDSS J134811.25+193523.6, 00087222001–00087222007 for SDSS J153533.88+025423.3, 00032624001–00032624003 for PMN J2134–0419, 00087543001–00087543018 (excluding 00087543013 because it lacks PC-mode exposures) for SDSS J161216.75+470253.6, and 00032626001–00032626005 for SDSS J222032.50+002537.5.

^c For archival XRT data, this column refers to the LIVETIME from the merged event lists. For archival EPIC data, this column refers to the LIVETIME of the EPIC-pn CCD on which the source is detected, after filtering background flares.

^d This column indicates whether the quasar is included in the flux-limited (FL) sample or not.

^e References. (1) Amirkhanyan & Mikhailov (2006); (2) Hook et al. (2002).

Table 2. HRLQs at $z > 4$ without available sensitive archival X-ray data.

Object Name	R.A. (J2000) (deg)	Dec. (J2000) (deg)	z	m_i	M_i	$f_{1.4\text{ GHz}}$ (mJy)	$\log R$
SDSS J082511.60+123417.2	126.2984	12.5715	4.378	20.71	–26.46	16.7	2.66
SDSS J094004.80+052630.9 ^a	145.0200	5.4419	4.503	20.80	–26.44	55.7	3.22
SDSS J104742.57+094744.9	161.9274	9.7958	4.252	20.29	–26.77	18.9	2.58
SDSS J115605.44+444356.5	179.0227	44.7324	4.310	21.06	–26.08	66.2	3.41
SDSS J125300.15+524803.3	193.2506	52.8009	4.115	21.33	–25.66	55.9	3.47
SDSS J140025.40+314910.6 ^a	210.1059	31.8196	4.640	20.28	–26.89	20.2	2.61
SDSS J153830.71+424405.6	234.6280	42.7349	4.099	20.77	–26.18	11.7	2.58
SDSS J154824.01+333500.1 ^a	237.1001	33.5834	4.678	20.35	–26.80	37.6	2.93
SDSS J165539.74+283406.7	253.9156	28.5685	4.048	20.42	–26.51	23.0	2.73

^a *Chandra*/ACIS observations have been conducted or scheduled for SDSS J094004.80+052630.9, SDSS J140025.40+314910.6, and SDSS J154824.01+333500.1. Their X-ray data will become public after their proprietary periods.

s^{-1} or better in the observed-frame 0.5–2 keV band) have been studied in Wu13 while another two were studied by Sbarrato et al. (2015). The other five objects (see Table 2 of Wu13) with $m_i < 21$ and lacking sensitive X-ray coverage

were awarded *Chandra* time in Cycle 17. The remaining two objects are fainter than $m_i = 21$. See Table 1 for the *Chandra* Cycle 17 observation log.⁵

We furthermore searched in the SDSS quasar catalog

spectral fitting (Shen et al. 2011) instead of m_i . We have thus revised the Wu13 sample from 28 objects to 26 objects.

⁵ SDSS J003126.79+150739.5 and SDSS J123142.17+381658.9 were also awarded *Chandra* time in Cycle 17. We analyze their

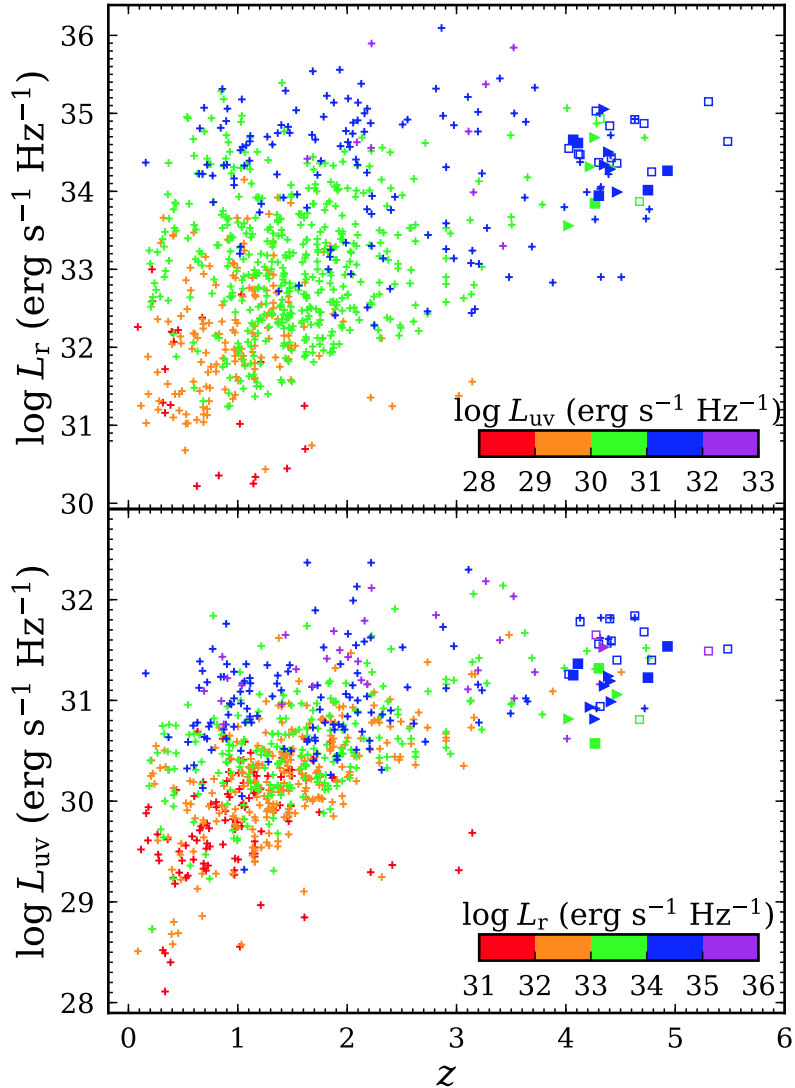


Figure 4. The radio (rest-frame 5 GHz; upper panel) and UV (rest-frame 2500 Å; lower panel) luminosities, plotted against redshift. The filled squares and triangles are the *Chandra* Cycle 17 objects and archival-data objects, respectively. The open squares are the high-redshift HRLQs of Wu13. The plus signs are the radio-loud and radio-intermediate objects in the full sample of Miller11. The upper and lower panels are color-coded based on UV and radio luminosity, respectively. Due to selection on R and m_i , our sample and the sample of Wu13 are composed of among the most-luminous objects in both the radio and UV bands.

Data Release 14 (DR14; Pâris et al. 2018) for HRLQs at $z = 4.0$ – 5.5 , and found another 16 HRLQs that were matched to the Faint Images of the Radio Sky at Twenty-centimeters survey (FIRST; Becker et al. 1995), which is designed to coincide with the primary region of sky covered by the SDSS. Since the FIRST survey has a detection limit of ≈ 1 mJy, all additional HRLQs in the SDSS quasar catalog DR14 with $m_i < 21$ can be detected by FIRST if they satisfy the criterion of $\log R > 2.5$.⁶ Another high- z HRLQ, B3 0254+434 (Amirkhanyan & Mikhailov 2006), was selected in NED using the same method as Wu13. See Section 3.5 for details on

the calculations of optical and radio luminosities and radio-loudness parameters using optical and radio fluxes. We retrieved the available sensitive archival X-ray observations from HEASARC⁷ of these new objects. Five high- z HRLQs (SDSS J083549.42+182520.0, SDSS J111323.35+464524.3, SDSS J134811.25+193523.6, SDSS J153533.88+025423.3, and SDSS J161216.75+470253.6) have useful deep ($\gtrsim 25$ ks) *Swift* X-ray observations. Two more (SDSS J102107.57+220921.4 and SDSS J160528.21+272854.4) are matched with the *XMM-Newton* serendipitous-source catalog 3XMM-DR8 (Rosen et al. 2016). See Table 1 for the observation log of the relevant *Swift* and *XMM-Newton* archival

X-ray data and report the results in Table 3, but will not show them in the figures or include them in the statistical tests.

⁶ The typical radio fluxes of the high- z HRLQs are $f_{1.4\text{GHz}} \geq 20$ mJy.

⁷ <https://heasarc.gsfc.nasa.gov/cgi-bin/W3Browse/w3browse.pl>

data.⁸ B3 0254+434 was awarded *Chandra* time in Cycle 17. The rest of the objects that lack publicly released sensitive archival X-ray observations are listed in Table 2.

We plotted the apparent *i*-band magnitudes and the X-ray coverage of all the HRLQs that were selected in this paper and in Wu13 in Fig. 2, where the objects with sensitive X-ray coverage were plotted as blue dots, while objects without sensitive X-ray coverage were plotted as blue circles. We here define our flux-limited high- z sample by applying an optical flux limit of $m_i \leq 20.26$. The 24 HRLQs that satisfy this flux cut all have sensitive X-ray coverage, among which 21 were selected in Wu13 and three (B3 0254+434, SDSS J134811.25+193523.6, and SDSS J153533.88+025423.3) were selected in this paper. In comparison with Wu13, our flux-limited sample is not only larger (twice as large) but also complete in its X-ray coverage (24/24 vs. 12/15), thus suffering less from selection biases. For comparison, the optical flux limit of the Wu13 flux-limited sample was $m_i = 20$.

We have plotted the rest-frame UV spectra for the members of our sample of HRLQs that are in the SDSS quasar catalogs in Fig. 3. It is apparent from their spectra that all of them are broad-line quasars, instead of BL Lac objects; the observed emission from the accretion disk and broad emission-line region in the optical/UV is free from strong contamination by boosted jet emission. The rest-frame UV spectra of the objects that were not in the SDSS quasar catalogs can be found in Hook et al. (2002) for PMN J2134–0419 and PMN J2314+0201 and Amirkhanyan & Mikhalov (2006) for B3 0254+434. The spectra of these 3 object show features of broad-line quasars as well. We also plotted the radio and optical/UV luminosities of high- z HRLQs against general RLQs in Fig. 4; their monochromatic luminosities are among the highest in both the radio and optical/UV bands, with our sample extending to a slightly fainter range than Wu13 in the optical/UV.

RLQs with extended radio morphologies have systematically larger radio-loudness parameters and also more powerful radio cores than quasars with compact radio morphologies (e.g. Lu et al. 2007). Our selection of HRLQs based on high R thus should not cause a bias toward including quasars with core-only morphologies or low intrinsic jet/core radio flux ratios, unless the cores dominate the radio fluxes for quasars with extended morphologies or RLQs jets evolve with redshift. High-redshift RLQs usually show compact radio morphology with few having apparently extended structures, which is probably due to the steeper radio slope ($\alpha_r < -0.5$) and the cosmological surface brightness dimming of diffuse radio emission, i.e., $(1+z)^{-4}$. Fifteen out of the 17 objects (except for B3 0254+434 and SDSS J1237+6517) in table 1 are within the footprint of the FIRST survey, and thirteen of them only show unresolved radio cores ($< 5''$, or < 35 kpc). The remaining two (SDSS J0813+3508 and SDSS J2220+0025) are resolved into multiple components (Becker et al. 1995; Hodge et al. 2011) and have a linear extent of $\approx 10''$ (≈ 70 kpc). The radio flux of the extended com-

ponent of SDSS J0813+3508 is about half that of the core, while the extended radio component is brighter than the core for SDSS J2220+0025. Several quasars in Table 1 have been observed using Very Long Baseline Interferometry (VLBI). Specifically, SDSS J0813+3508 and SDSS J1242+5422 were observed by Frey et al. (2010) at 1.6 GHz and 5 GHz, and PMN J2134–0419 and SDSS J2220+0025 were observed by Cao et al. (2017) at 1.7 GHz and 5 GHz. These observations can resolve structures on the scale of 1.2–25 milliarcseconds (≈ 8 –160 pc). At such small scales, these quasars are often mildly resolved and show a compact core with a one-sided jet (SDSS J0813+3508 and PMN J2134–0419) or an unresolved core (SDSS J1242+5422 and SDSS J2220+0025). Note that VLBI observation of PMN J2314–0419 shows evidence of strong Doppler boosting (Cao et al. 2017).

3 X-RAY DATA ANALYSES AND MULTI-WAVELENGTH PROPERTIES

In the below, we define the soft band, hard band, and full band to be 0.5–2 keV, 2.0–8.0 keV, and 0.5–8 keV in the observed frame, respectively.

3.1 *Chandra* data analyses

Eight RLQs were targeted with the Advanced CCD Imaging Spectrometer (ACIS; Garmire et al. 2003) onboard *Chandra*, using the back-illuminated S3 chip. The *Chandra* data (see Table 1) were first reprocessed using the standard CIAO (v4.9) routine CHANDRA_REPRO and the latest CALDB (v4.7.3). X-ray images and exposure maps were then generated using FLUXIMAGE in the three observed bands, where the effective energy that was used to calculate the exposure map was chosen to be the geometric mean of the limits of each band. All of the sources were detected by WAVDETECT (Freeman et al. 2002) in at least two bands with a detection threshold 10^{-6} and wavelet scales of 1, $\sqrt{2}$, 2, $2\sqrt{2}$, and 4 pixels. We performed statistical tests on the X-ray images and found no extended structure or large-scale jets. Furthermore, we constrained any extended X-ray jets to be $\gtrsim 3$ –25 times fainter than the cores. (see details in Appendix A). Raw source and background counts were extracted using DMEXTRACT. The source region was a circle with a radius of $2.0''$, centred at the X-ray position from WAVDETECT, and the background region was a concentric annulus with an inner radius of $5.0''$ and an outer radius of $20.0''$. The offset between the X-ray position and optical position of each source ranges from $0.2''$ to $0.7''$. All the background regions are free of X-ray sources except for that of SDSS J123142.17+381658.9, in which we have excluded a source detected by WAVDETECT. The circular source region encloses $\approx 95.9\%$ of the total energy at 1 keV and $\approx 90.6\%$ of the total energy at 4 keV.⁹ We also extracted source and background spectra using SPEXTRACT,¹⁰ which simultaneously produces response matrix files (RMFs) and ancillary response files (ARFs).¹¹

⁸ PMN J2134–0419 and SDSS J222032.50+002537.5 were selected by Wu13, and their archival X-ray data have been analyzed by Sbarrato et al. (2015); we analyzed the same data here to maintain consistency with the other objects.

⁹ http://cxc.harvard.edu/ciao/ahelp/src_psffrac.html

¹⁰ We used a larger background region to enclose more background events in extracting background spectra.

¹¹ Including both aperture-corrected and uncorrected ARFs.

Table 3. X-ray net counts, hardness ratio, and effective photon index.

Object Name	Net X-ray Counts			Band Ratio ^a	Γ_X
	Full Band (0.5–8 keV)	Soft Band (0.5–2 keV)	Hard Band (2–8 keV)		
<i>Chandra Cycle 17 Objects</i>					
SDSS J003126.79+150739.5	14.8 ^{+4.4} _{-3.6}	12.5 ^{+4.0} _{-3.3}	2.1 ^{+2.0} _{-1.3}	0.17 ^{+0.09} _{-0.14}	2.43 ^{+1.20} _{-0.33}
B3 0254+434	110.6 ^{+11.2} _{-10.5}	60.4 ^{+8.3} _{-7.6}	50.7 ^{+7.8} _{-7.1}	0.84 ^{+0.13} _{-0.20}	1.44 ^{+0.21} _{-0.11}
SDSS J030437.21+004653.5	10.5 ^{+3.8} _{-3.0}	9.4 ^{+3.5} _{-2.8}	< 4.1	< 0.44	> 1.79
SDSS J081333.32+350810.8	28.7 ^{+5.9} _{-5.2}	16.6 ^{+4.6} _{-3.8}	12.1 ^{+4.0} _{-3.3}	0.73 ^{+0.19} _{-0.32}	1.35 ^{+0.44} _{-0.17}
SDSS J123142.17+381658.9	25.3 ^{+5.5} _{-4.9}	15.6 ^{+4.4} _{-3.7}	9.8 ^{+3.7} _{-3.0}	0.63 ^{+0.21} _{-0.29}	1.37 ^{+0.44} _{-0.21}
SDSS J123726.26+651724.4	13.6 ^{+4.2} _{-3.5}	10.4 ^{+3.7} _{-3.0}	3.1 ^{+2.4} _{-1.6}	0.30 ^{+0.16} _{-0.21}	1.92 ^{+0.90} _{-0.30}
SDSS J124230.58+542257.3	15.8 ^{+4.5} _{-3.8}	13.5 ^{+4.1} _{-3.3}	2.1 ^{+2.0} _{-1.3}	0.16 ^{+0.09} _{-0.12}	2.38 ^{+1.13} _{-0.33}
PMN J2314+0201	43.5 ^{+7.2} _{-6.5}	25.0 ^{+4.9} _{-4.8}	18.6 ^{+4.9} _{-4.2}	0.74 ^{+0.20} _{-0.25}	1.33 ^{+0.30} _{-0.17}
<i>Archival Data Objects</i>					
SDSS J083549.42+182520.0	205.2 ^{+17.1} _{-16.9}	135.3 ^{+13.9} _{-13.3}	69.8 ^{+10.5} _{-10.1}	0.52 ^{+0.08} _{-0.09}	1.56 ^{+0.15} _{-0.10}
SDSS J102107.57+220921.4	49.8 ^{+13.9} _{-14.2}	37.7 ^{+9.6} _{-9.4}	< 26.6	< 0.71	> 1.30
SDSS J111323.35+464524.3	33.3 ^{+8.2} _{-7.5}	21.9 ^{+6.6} _{-5.9}	11.4 ^{+5.1} _{-4.4}	0.52 ^{+0.17} _{-0.29}	1.51 ^{+0.59} _{-0.21}
SDSS J134811.25+193523.6	78.4 ^{+12.7} _{-12.0}	52.5 ^{+10.5} _{-9.8}	26.0 ^{+7.4} _{-6.8}	0.49 ^{+0.14} _{-0.17}	1.56 ^{+0.32} _{-0.18}
SDSS J153533.88+025423.3	324.3 ^{+21.7} _{-21.5}	185.7 ^{+16.9} _{-16.3}	138.6 ^{+14.2} _{-13.7}	0.75 ^{+0.08} _{-0.10}	1.32 ^{+0.11} _{-0.08}
SDSS J160528.21+272854.4	< 61.5	26.8 ^{+10.9} _{-10.8}	< 28.4	-	-
SDSS J161216.75+470253.6	23.1 ^{+6.6} _{-6.0}	19.1 ^{+5.7} _{-5.0}	< 10.1	< 0.53	> 1.50
PMN J2134-0419	70.7 ^{+11.2} _{-10.7}	49.3 ^{+9.1} _{-8.5}	21.4 ^{+7.0} _{-6.2}	0.43 ^{+0.12} _{-0.18}	1.70 ^{+0.38} _{-0.18}
SDSS J222032.50+002537.5	44.8 ^{+9.7} _{-9.2}	37.6 ^{+8.2} _{-7.6}	< 15.8	< 0.42	> 1.76

^a The band ratio here refers to the number of hard-band counts divided by the number of the soft-band counts.

3.2 *Swift* data analyses

Data reduction of the *Swift*/X-ray Telescope (XRT; Burrows et al. 2005) observations was performed using standard routines in FTOOLS integrated in HEASoft (v6.21).¹² Each HRLQ has multiple observations (see Table 1). For each observation, the cleaned event list and exposure map were created using XRTPipeline and XRTEX-POMAP, respectively. We only used XRT data in photon-counting (PC) mode. The event lists and exposure maps of different observations were then merged using XSELECT and XIMAGE, respectively. We extracted photons in the three bands from circular regions centred at the source positions with radii of $\sim 60''$ except for SDSS J111323.35+464524.3 and SDSS J161216.75+470253.6, for which we have adopted a radius of $25''$ to avoid contamination by nearby sources. These source-extraction regions enclose ~ 80 – 90% (73% for SDSS J111323.35+464524.3 and 80% for SDSS J161216.75+470253.6) of the total energy at 1 keV. Photons from circular source-free regions of radii that are more than twice as large as the source region were extracted to estimate the background level. We also extracted source and background spectra using XSELECT, and created ARFs using XRTMKARF, which simultaneously provides the corresponding RMFs.

3.3 *XMM-Newton* data analyses

SDSS J102107.57+220921.4 and SDSS J160528.21+272854.4 were serendipitously observed by *XMM-Newton* (see Table 1).¹³ Data reduction was performed using SAS (v16.1.0) and the latest Current Calibration Files (as of 2018 March). We only utilized the data from the pn CCDs of the European Photon Imaging Camera (EPIC-pn; Strüder et al. 2001) onboard *XMM-Newton*. The data were reprocessed and cleaned using EPPROC, and high-background flaring periods were filtered using ESPFILT. We created images and exposure maps using EVSELECT and EEXPMAP and then performed source detection using EBOXDETECT.¹⁴ Both targets were detected in the full and soft bands, and the offsets between the X-ray positions and optical positions are $\sim 1''$ – $2''$ (Rosen et al. 2016). We extracted photons from source regions that are defined by a circle with a radius of $40''$, centred at the optical position. Background photons were extracted from source-free circular regions on the same chips, with radii of $60''$ and $50''$ for SDSS J102107.57+220921.4 and SDSS J160528.21+272854.4, respectively. The encircled-energy fraction is $\approx 86\%$ for both sources at 1 keV, which is calculated using the point spread function (PSF) images created by PSFGEN. We also extracted spectra using EVSELECT and created corresponding RMFs and ARFs using RMFGEN and ARFGEN, respectively.

¹³ These two serendipitously observed HRLQs are near to the edges of the EPIC-pn CCDs, with off-axis angles of $\approx 15'$ – $17'$.¹⁴ <https://www.cosmos.esa.int/web/xmm-newton/sas-thread-src-find-stepbystep>¹² <https://heasarc.nasa.gov/lheasoft/>

3.4 Source detection and photometry

In the below, analyses of *Chandra*/ACIS, *Swift*/XRT, and *XMM-Newton*/EPIC data were conducted in a unified way. Using the raw source and background event counts, we calculated the binomial no-source probability (referred to as P_B in this paper; Weisskopf et al. 2007)¹⁵ to test the significance of the source signal in each band, and took cases with $P_B \leq 0.01$ as detections. We calculated net counts from the HRLQs (with aperture corrections) and their 1σ intervals using APRATES¹⁶ within CIAO. For each band without a detection ($P_B > 0.01$), we gave a 90% confidence upper limit (Kraft et al. 1991).

We then proceeded by calculating the hardness ratio of each source. The 68% bounds of hardness ratio were calculated using the Bayesian approach of Park et al. (2006). Using the response files and MODELFLUX (another CIAO routine),¹⁷ we calculated the expected HRs of Galactic-absorbed power-law spectra with a range of photon indices, from which we calculated the effective power-law photon index (Γ_X) of each source. The results of the photometry are listed in Table 3. SDSS J124230.58+542257.3 has a noticeably large effective photon index, and deeper X-ray observations in the future might help to improve our understanding of it.¹⁸

¹⁵ P_B is the chance probability of observing a signal no weaker than the source counts under the null hypothesis that there is no source in the source-extraction region. Thus, it is essentially a p -value.

¹⁶ <http://cxc.harvard.edu/ciao/ahelp/aprates.html> and <http://cxc.harvard.edu/ciao/threads/aprates/>

¹⁷ See <http://cxc.harvard.edu/ciao/ahelp/modelflux.html> and <http://cxc.harvard.edu/ciao/why/pimms.html>. Since we have obtained response files for all the observations, we also use MODELFLUX with *XMM-Newton* and *Swift* data.

¹⁸ SDSS J003126.79+150739.5 with $\log R = 2.44$ does not strictly satisfy our definition for HRLQs, but it has an even steeper effective photon index.

Table 4. X-ray, optical/UV, and radio properties.

Object Name (1)	m_i (2)	M_i (3)	N_H^a (4)	C.R. ^b (5)	F_X^c (6)	$f_{2\text{keV}}^d$ (7)	$\log L_X^e$ (8)	Γ_X^f (9)	$f_{2500\text{\AA}}^g$ (10)	$\log L_{2500\text{\AA}}^h$ (11)	α_r^i (12)	$\log L_r^j$ (13)	$\log R$ (14)	α_{ox} (15)	$\Delta\alpha_{\text{ox,RQQ}}^k$ (16)	$\Delta\alpha_{\text{ox,RLQ}}^l$ (17)
<i>Chandra</i> Cycle 17 Objects																
SDSS J003126.79+150739.5	19.99	-27.16	4.43	$2.33^{+0.74}_{-0.61}$	1.81	21.17	45.61	$2.43^{+1.20}_{-0.33}$	0.92	31.50	0.61	34.07	2.44	-1.40	0.31	0.10
B3 0254+434	20.01	-27.24	13.45	$10.96^{+1.50}_{-1.38}$	7.98	34.94	46.14	$1.44^{+0.21}_{-0.11}$	0.56	31.25	0.06	34.66	3.29	-1.23	0.44	0.15
SDSS J030437.21+004653.5	20.15	-27.09	7.26	$1.60^{+0.60}_{-0.48}$	1.10	7.03	45.35	> 1.79	0.11	30.57	-	33.85	3.15	-1.23	0.35	0.11
SDSS J081333.32+350810.8	19.15	-28.30	4.91	$2.78^{+0.76}_{-0.64}$	1.72	7.27	45.63	$1.35^{+0.44}_{-0.17}$	0.81	31.54	-0.60	34.26	2.61	-1.55	0.16	-0.07
SDSS J123142.17+381658.9	20.12	-26.88	1.27	$2.58^{+0.73}_{-0.61}$	1.52	6.22	45.43	$1.37^{+0.45}_{-0.19}$	1.13	31.56	-	33.82	2.14	-1.63	0.08	-0.10
SDSS J123726.26+651724.4	20.46	-26.63	2.03	$1.32^{+0.47}_{-0.38}$	0.90	6.59	45.28	$1.92^{+0.90}_{-0.30}$	0.61	31.32	-	33.94	2.50	-1.52	0.16	-0.05
SDSS J124230.58+542257.3	19.65	-27.63	1.55	$2.77^{+0.84}_{-0.71}$	1.73	21.96	45.71	$2.38^{+1.13}_{-0.33}$	0.42	31.23	-0.56	34.01	2.67	-1.24	0.43	0.21
PMN J2314+0201	19.54	-27.41	4.82	$4.25^{+0.93}_{-0.81}$	2.64	10.36	45.67	$1.33^{+0.33}_{-0.15}$	0.72	31.36	-0.27	34.62	3.13	-1.47	0.21	-0.06
Archival Data Objects																
SDSS J083549.42+182520.0	20.74	-26.47	3.21	$2.95^{+0.29}_{-0.30}$	6.17	31.74	46.11	$1.56^{+0.15}_{-0.11}$	0.27	30.99	-0.20	34.30	3.19	-1.12	0.51	0.25
SDSS J102107.57+220921.4	21.03	-26.04	2.03	$4.65^{+1.19}_{-1.16}$	2.72	14.32	45.73	> 1.30	0.19	30.81	-0.17	34.69	3.75	-1.20	0.41	0.10
SDSS J111323.35+464524.3	20.58	-26.65	1.31	$0.63^{+0.15}_{-0.12}$	0.95	4.64	45.30	$1.51^{+0.59}_{-0.21}$	0.31	31.06	-0.17	33.99	2.81	-1.47	0.17	-0.05
SDSS J134811.25+193523.6	20.21	-26.98	1.93	$1.13^{+0.23}_{-0.21}$	2.29	11.75	45.68	$1.56^{+0.34}_{-0.17}$	0.44	31.19	-0.20	34.28	2.97	-1.37	0.29	0.04
SDSS J153533.88+025423.3	20.08	-27.10	4.44	$7.03^{+0.64}_{-0.62}$	15.13	59.82	46.48	$1.32^{+0.10}_{-0.09}$	0.49	31.24	-0.31	34.50	3.14	-1.12	0.55	0.28
SDSS J160528.21+272854.4	20.85	-26.04	3.94	$2.44^{+0.99}_{-0.98}$	1.59	8.12	45.44	-	0.21	30.82	-	33.56	2.62	-1.31	0.30	0.10
SDSS J161216.75+470253.6	20.29	-26.86	1.33	$0.39^{+0.12}_{-0.10}$	0.79	4.19	45.21	> 1.50	0.40	31.14	-0.44	34.34	3.07	-1.53	0.13	-0.13
PMN J2134-0419	19.30	-27.84	3.55	$1.96^{+0.36}_{-0.34}$	4.19	24.66	45.94	$1.70^{+0.38}_{-0.18}$	0.96	31.53	-0.23	35.05	3.40	-1.38	0.33	0.02
SDSS J222032.50+002537.5	19.95	-27.20	4.73	$0.86^{+0.19}_{-0.17}$	1.85	11.36	45.56	> 1.76	0.26	30.93	-	34.32	3.26	-1.29	0.34	0.07

^a Galactic neutral hydrogen column density in units of 10^{20} cm^{-2} .

^b Count rate of the in the observed-frame 0.5–2 keV band, in units of 10^{-3} s^{-1} .

^c Galactic absorption-corrected flux in the observed-frame 0.5–2 keV band, in units of $10^{-14} \text{ erg cm}^{-2} \text{ s}^{-1}$.

^d Flux density at $2/(1+z)$ keV (extrapolated from the observed 0.5–8 keV X-ray emission), in units of $10^{-32} \text{ erg cm}^{-2} \text{ s}^{-1} \text{ Hz}^{-1}$.

^e The logarithm of the X-ray luminosity in the rest-frame 2–10 keV band, in units of erg s^{-1} .

^f Effective X-ray power-law photon index.

^g Flux density observed at $2500(1+z) \text{ \AA}$ in units of $10^{-27} \text{ erg cm}^{-2} \text{ s}^{-1} \text{ Hz}^{-1}$.

^h Logarithm of the monochromatic UV luminosity at rest frame 2500 \AA in units of $\text{erg s}^{-1} \text{ Hz}^{-1}$.

ⁱ Radio spectral index calculated from observed 1.4 GHz and 5 GHz flux, defined as $f_r \propto \nu^{\alpha_r}$. If a 5 GHz observation is absent, we take $\alpha_r = 0$ in the following calculation. The radio spectral index of SDSS J0813+3508 is from Frey et al. (2010).

^j Logarithm of the monochromatic radio luminosity at rest-frame 5 GHz in units of $\text{erg s}^{-1} \text{ Hz}^{-1}$.

^k The difference between the measured α_{ox} and the expected α_{ox} for RQQs with similar UV luminosity, defined by Eq. (3) of Just et al. (2007).

^l The difference between the measured α_{ox} and the expected α_{ox} for RLQs with similar UV and radio luminosities, defined by the $L_{2\text{keV}}-L_{2500\text{\AA}}-L_{5\text{GHz}}$ relation in Table 7 of Miller et al. (2011).

3.5 X-ray, optical/UV, and radio properties

In Table 4, we summarize the X-ray, optical/UV, and radio properties of our sample of HRLQs, utilizing the results of our X-ray data analyses as well as SDSS and FIRST/NVSS surveys. We explain the content of each column below:

Column (1): the name of the quasar.

Column (2): the apparent i -band magnitude of the quasar.

Column (3): the absolute i -band magnitude of the quasar. The values are preferentially taken from SDSS quasar catalogs (Schneider et al. 2010; Pâris et al. 2018). For objects that are not in the quasar catalogs, we calculated M_i from m_i by correcting for the Galactic extinction (Schlafly & Finkbeiner 2011) and using the K-correction in Section 5 of Richards et al. (2006).

Column (4): the Galactic neutral hydrogen column density (Dickey & Lockman 1990; Stark et al. 1992).¹⁹

Column (5): the count rate in the observed-frame soft X-ray band for the *Chandra* Cycle 17 objects.

Column (6): the observed X-ray flux in the soft band calculated using MODELFLUX, the effective power-law photon index (see Column 9), and the instrumental response files. The values have been corrected for Galactic absorption.

Column (7): following Wu13, in this column we estimated the observed X-ray flux density at $2/(1+z)$ keV (i.e. rest-frame 2 keV), corrected for Galactic absorption. Note that, for objects at $z > 4$, the rest-frame 2 keV X-rays are below the lower limit of our observed X-ray bands. Thus, we have extrapolated their X-ray spectra using the effective power-law photon index (see Column 9) to lower energies. Note that this is a relatively short extrapolation, generally a factor of $\lesssim 1.5$ times below the lowest energy of our observed X-rays. Column (8): the logarithm of the rest-frame 2–10 keV luminosity.

Column (9): the effective power-law photon index in the X-ray band. For the sources with only a lower limit or without estimation of Γ_X , we have adopted a typical value for RLQs ($\Gamma_X = 1.6$; e.g. Page et al. 2005), and for SDSS J030437.21+004653.5 and SDSS J161216+470253.6 we have used their lower limits ($\Gamma_X = 1.79$ and 1.76) in the following analysis. Within a reasonable range ($\Gamma_X = 1.4$ – 1.9 ; e.g. Page et al. 2005), the value of Γ_X does not materially affect the results we presented below.

Column (10): the observed flux density at $2500(1+z)$ Å (i.e. rest-frame 2500 Å). For objects in the SDSS DR7 quasar catalog, the values were taken from Shen et al. (2011). For other objects, the values were calculated from their i -band magnitude (Column 3).

Column (12): the radio spectral index α_r ($f_\nu \propto \nu^{\alpha_r}$) between observed-frame 1.4 GHz and 5 GHz. We obtain 1.4 GHz flux densities from the FIRST or NVSS surveys. The 5 GHz flux densities were mostly from the Green Bank 6-cm survey (Gregory et al. 1996). We obtain the 5 GHz flux density of PMN J2134–0419 from the Parkes-MIT-NRAO survey (Wright et al. 1994). We took the 5 GHz flux density of SDSS J124230.58+542257.3 from its VLBI observation (Frey et al. 2010). The radio counterpart of SDSS J081333.32+350810.8 has a close companion ($\sim 6''$) in the FIRST catalog, which cannot be identified in the optical and is likely to be associated with SDSS J081333.32+350810.8 as

a jet or lobe. We thus took the 1.4 GHz flux density of SDSS J081333.32+350810.8 as the sum of the two radio sources from the FIRST catalog. Since the radio companion is completely resolved in VLBI imaging, we take $\alpha_r = -0.6$ from Frey et al. (2010).

Column (13): the logarithm of the monochromatic luminosity at rest-frame 5 GHz, in units of $\text{erg s}^{-1} \text{Hz}^{-1}$. We calculated $\log L_r$ using the observed-frame 1.4 GHz flux and radio spectral index (α_r ; see Column 12).

Column (14): the logarithm of the radio-loudness parameter, given by

$$\log R = \log \left(\frac{f_{5 \text{ GHz}}}{f_{4400 \text{ \AA}}} \right) \quad (1)$$

$$= \log \left(\frac{L_r}{L_{2500 \text{ \AA}}} \right) - 0.5 \log \left(\frac{4400}{2500} \right), \quad (2)$$

where we have calculated the rest-frame 4400 Å flux density (monochromatic luminosity) using the rest-frame 2500 Å flux density (monochromatic luminosity) and an assumed optical spectral index $\alpha = -0.5$ (e.g. Vanden Berk et al. 2001).

Column (15): the two-point spectral index α_{ox} (Tananbaum et al. 1979), defined by

$$\alpha_{\text{ox}} = \frac{\log(f_2 \text{ keV} / f_{2500 \text{ \AA}})}{\log(\nu_2 \text{ keV} / \nu_{2500 \text{ \AA}})}, \quad (3)$$

which represents the spectral index of an assumed power-law connecting rest-frame 2500 Å and 2 keV.

Column (16): the difference between the measured α_{ox} of our quasar and the expected α_{ox} for a typical RQQ using the $\alpha_{\text{ox}}-L_{2500 \text{ \AA}}$ relation in Eq. 3 of Just et al. (2007),

$$\Delta\alpha_{\text{ox,RQQ}} = \alpha_{\text{ox}} - \alpha_{\text{ox,RQQ}}. \quad (4)$$

$\Delta\alpha_{\text{ox,RQQ}}$ quantifies the amount of additional X-ray emission from the jet-component of RLQs compared to the X-ray emission of RQQs.

Column (17): the difference between the measured α_{ox} of our quasar at $z > 4$ and the expected α_{ox} for a typical low-redshift RLQ (mostly at $z = 0.3$ – 2.5 with a median of $z = 1.4$) using the $L_2 \text{ keV}-L_{2500 \text{ \AA}}-L_5 \text{ GHz}$ relation in Table 7 of Miller11,

$$\Delta\alpha_{\text{ox,RLQ}} = \alpha_{\text{ox}} - \alpha_{\text{ox,RLQ}}. \quad (5)$$

4 X-RAY ENHANCEMENTS OF HIGH-REDSHIFT HRLQs

In this section, we perform statistical tests on the $\Delta\alpha_{\text{ox}}$ distributions of HRLQs at $z > 4$ against those of their low-redshift counterparts, using the enlarged and complete sample, compared with Wu13 (see Section 2). We quantify the typical excess of jet-linked X-ray emission using the medians of $\Delta\alpha_{\text{ox}}$ distributions. The relevant properties of the flux-limited high- z sample of HRLQs are compiled in Table 5.

4.1 Basic comparisons

We first plot α_{ox} , $\Delta\alpha_{\text{ox,RQQ}}$, and $\Delta\alpha_{\text{ox,RLQ}}$ for all the high- z HRLQs with sensitive X-ray coverage against their $\log R$ in Fig. 5, where the filled squares, filled triangles, and open

¹⁹ <http://cxc.harvard.edu/toolkit/colden.jsp>

Table 5. HRLQs at $z > 4$ that are analyzed in this paper and from Wu13 (32 objects in total).

Object Name	z	m_i	M_i	$\log R^a$	α_r^b	α_{ox}	$\Delta\alpha_{\text{ox,RQQ}}$	$\Delta\alpha_{\text{ox,RLQ}}$	Factor ^c	FL ^d
From this paper (15 objects)										
B3 0254+434	4.067	20.01	-27.13	3.29	0.06	-1.23	0.44	0.15	2.46	Y
SDSS J030437.21+004653.5	4.266	20.15	-27.09	3.15	-	-1.23	0.35	0.11	1.93	Y
SDSS J081333.32+350810.8	4.929	19.15	-28.30	2.61	-0.60	-1.55	0.16	-0.07	0.66	Y
SDSS J124230.58+542257.3	4.750	19.65	-27.63	2.67	-0.56	-1.24	0.43	0.21	3.53	Y
SDSS J134811.25+193523.6	4.404	20.20	-26.98	2.97	-0.20	-1.37	0.29	0.04	1.27	Y
SDSS J153533.88+025423.3	4.388	20.07	-27.10	3.14	-0.31	-1.12	0.55	0.28	5.36	Y
PMN J2134-0419	4.346	19.30	-27.82	3.40	-0.23	-1.38	0.33	0.02	1.13	Y
SDSS J222032.50+002537.5	4.220	19.95	-27.20	3.26	-	-1.35	0.31	0.04	1.27	Y
PMN J2314+0201	4.110	19.54	-27.41	3.13	-0.27	-1.47	0.21	-0.06	0.70	Y
SDSS J083549.42+182520.0	4.412	20.74	-26.47	3.19	-0.20	-1.12	0.51	0.25	4.48	N
SDSS J102107.57+220921.4	4.262	21.03	-26.04	3.75	-0.17	-1.20	0.41	0.10	1.82	N
SDSS J111323.35+464524.3	4.468	20.58	-26.65	2.81	-0.17	-1.53	0.11	-0.05	0.74	N
SDSS J123726.26+651724.4	4.301	20.46	-26.63	2.50	-	-1.52	0.16	-0.05	0.74	N
SDSS J160528.21+272854.4	4.024	20.85	-26.04	2.61	-	-1.31	0.30	0.10	1.82	N
SDSS J161216.75+470253.6	4.350	20.29	-26.86	3.07	-0.44	-1.53	0.13	-0.13	0.46	N
From Wu13 (17 objects)										
PSS 0121+0347	4.130	18.57	-28.44	2.57	-0.33	-1.47	0.28	0.04	1.27	Y
PMN J0324-2918	4.630	18.65	-28.61	2.95	0.30	-1.40	0.35	0.08	1.62	Y
PMN J0525-3343	4.401	18.63	-28.52	2.90	0.06	-1.17	0.58	0.31	6.42	Y
Q0906+6930	5.480	19.85	-27.76	3.01	0.17	-1.31	0.40	0.13	2.18	Y
SDSS J102623.61+254259.5	5.304	20.03	-27.50	3.54	-0.38	-1.31	0.39	0.07	1.52	Y
RX J1028.6-0844	4.276	19.14	-27.95	3.33	-0.30	-1.09	0.63	0.34	7.69	Y
PMN J1155-3107	4.300	19.28	-27.90	2.73	0.53	-1.36	0.36	0.12	2.05	Y
SDSS J123503.03-000331.7	4.673	20.10	-27.20	3.05	-	-1.22	0.39	0.16	2.61	Y
CLASS J1325+1123	4.415	19.18	-28.01	2.72	-0.09	-1.53	0.19	-0.05	0.74	Y
SDSS J141209.96+062406.9	4.467	19.44	-27.74	2.70	-	-1.51	0.18	-0.06	0.70	Y
SDSS J142048.01+120545.9	4.027	19.80	-27.18	3.05	-0.36	-1.34	0.33	0.06	1.43	Y
GB 1428+4217	4.715	19.10	-28.18	3.06	0.37	-0.93	0.80	0.52	22.6	Y
GB 1508+5714	4.313	19.92	-27.16	3.87	0.13	-0.96	0.67	0.34	7.69	Y
SDSS J165913.23+210115.8	4.784	20.26	-27.17	2.56	-	-1.39	0.30	0.07	1.52	Y
PMN J1951+0134	4.114	19.69	-27.40	3.04	0.24	-1.23	0.45	0.20	3.32	Y
SDSS J091316.55+591921.6 ^e	5.122	20.39	-27.03	2.72	-0.67	-1.76	-0.09	-0.32	0.15	N
GB 1713+2148	4.011	21.42	-25.53	4.50	-0.30	-1.16	0.42	0.05	1.35	N

^a The objects are sorted in ascending order of RA.

^b The radio spectral index that is calculated using observed-frame 1.4 GHz and 5 GHz flux densities.

^c The factor of X-ray enhancement calculated using $10^{\Delta\alpha_{\text{ox,RLQ}}/0.3838}$.

^d This column indicates whether the object belongs to the flux-limited sample or not (see Section 2). The quasars that are outside the flux-limited sample are appended below the flux-limited sample, also in ascending order of RA.

^e We consider SDSS J091316.55+591921.6 as an outlier among the quasar sample.

squares represent *Chandra* Cycle 17 objects, archival data objects, and Wu13 objects, respectively. The median redshift of the high- z HRLQs is $z = 4.3$, and the interquartile (25th percentile to 75th percentile) range is [4.2, 4.4]. For comparison, also plotted in Fig. 5 are the radio-loud and radio-intermediate quasars in the full sample of Miller11²⁰ with a median redshift of $z = 1.4$ (and an interquartile range of [1.0, 1.9]). The loci of high- z HRLQs are not consistent with those of typical low- z RLQs in the three panels. Especially in the $\Delta\alpha_{\text{ox,RQQ}}\text{-}\log R$ and $\Delta\alpha_{\text{ox,RLQ}}\text{-}\log R$ planes, HRLQs at $z > 4$ have systematically larger $\Delta\alpha_{\text{ox,RQQ}}$ and $\Delta\alpha_{\text{ox,RLQ}}$.

We further compared the $\Delta\alpha_{\text{ox}}$ distribution of the

flux-limited sample (see Section 2) with that of their low- z counterparts using histograms. We thus define a flux-limited ($m_i \leq 20.26$) comparison sample of HRLQs at $z < 4$ that is a subset of the full sample of RLQs in Miller11. The high- z and low- z samples contain 24 and 311 objects, with median redshifts of 4.4 and 1.3 (and interquartile ranges of [4.3, 4.7] and [0.9, 1.8]), respectively.

In addition to the flux-limit and radio-loudness cuts we have applied, we confirmed that the quasars in the low- z sample show comparably strong emission lines to those in the high- z sample (i.e. they are largely free from strong boosted non-thermal continuum emission in the optical/UV; see Fig. 3). We first matched the low- z sample to the DR7 quasar property catalog (Shen et al. 2011) and checked the rest-frame equivalent widths (REWs) of H β , Mg II, and C IV. 187 quasars in the low- z sample are included in the DR7 quasar property catalog; all of them have at least one emis-

²⁰ Miller11 quantify radio loudness using the ratio of monochromatic luminosities at rest-frame 5 GHz and 2500 Å. We have converted their values of radio loudness to the values according to our definition, assuming $\alpha = -0.5$.

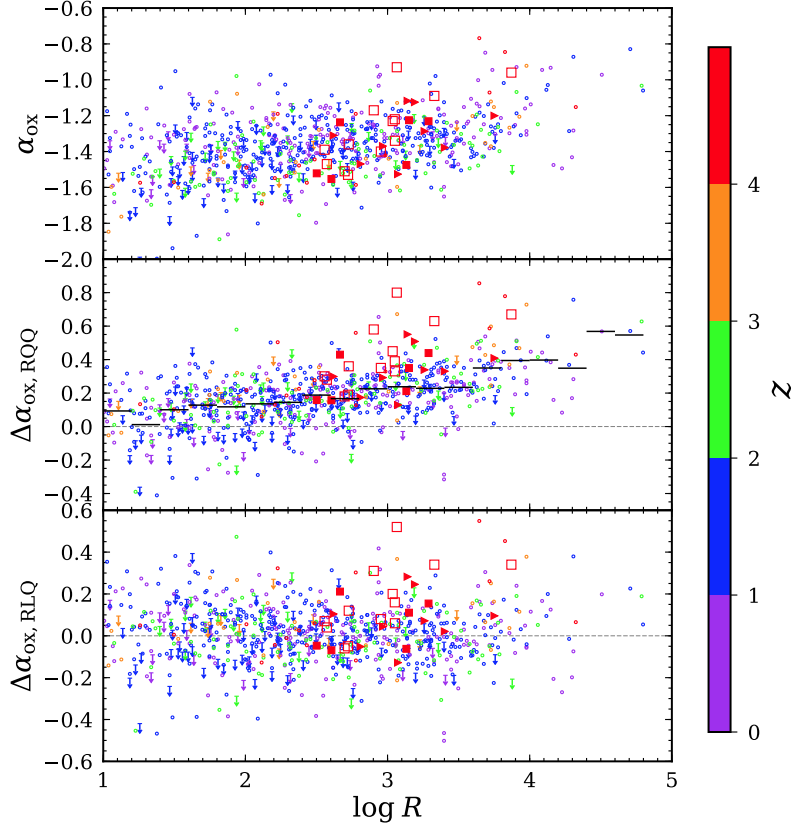


Figure 5. The relations between radio loudness ($\log R$) and α_{ox} , $\Delta\alpha_{\text{ox,RQQ}}$, and $\Delta\alpha_{\text{ox,RLQ}}$, from top to bottom. The filled squares and triangles are from the *Chandra* Cycle 17 objects and archival data objects, respectively. The open squares are from Wu13. The small open circles represent the radio-loud and radio-intermediate objects in the full sample of Miller11 that are detected in X-rays, while the downward arrows have only X-ray upper limits. The dashed lines label the positions of $\Delta\alpha_{\text{ox}} = 0$. The thick black lines in the middle panel are the mean $\Delta\alpha_{\text{ox,RQQ}}$ values for the Miller11 RLQs in $\log R$ bins ($\Delta\log R = 0.2$ per bin). All symbols are color-coded based on their redshifts using the color bar on the right-hand side.

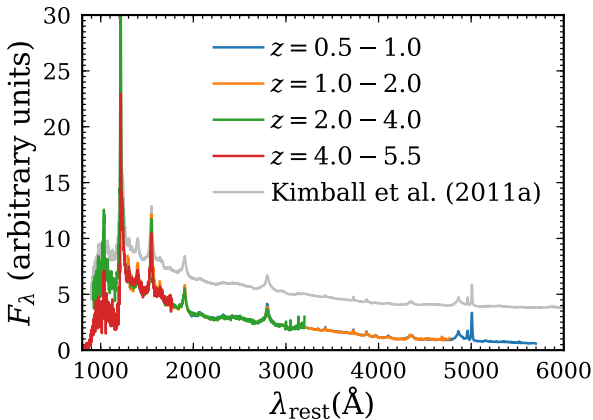


Figure 6. The composite SDSS spectra of HRLQs in different redshift bins. The quasars in bins of $z = 0.5-1.0$, $1.0-2.0$, and $2.0-4.0$ are from Miller11, and the quasars in the bin of $z = 4.0-5.5$ are from this paper. The grey curve (vertically shifted) is a composite spectrum of SDSS quasars that have radio counterparts with $f_{1.4 \text{ GHz}} \geq 2 \text{ mJy}$ (Kimball et al. 2011a). The composite spectra of HRLQs in different redshift bins match so well that it is hard to notice the overlapping (except that the $z = 4.0-5.5$ quasars suffer more severe absorption below the Lyman limit). The strengths of emission lines do not have an apparent dependence on redshift.

sion line (of the three we checked) that has $\text{REW} > 5 \text{ \AA}$. We also visually inspected the SDSS spectra of the 214 low- z quasars within the SDSS quasar catalog DR14 (P aris et al. 2018), and almost all of them show strong emission lines. To demonstrate the similarly strong emission lines in the high- z and low- z samples, we create composite SDSS spectra for the HRLQs in four redshift bins (quasars at $z < 0.5$ are discarded due to their largely different rest-frame wavelength ranges) and show them in Fig. 6. To create these composite spectra, each spectrum was first shifted to its rest frame and normalised to some continuum window (e.g. Vanden Berk et al. 2001), and then the median flux in each wavelength bin was calculated. It is apparent from the significant overlapping in Fig. 6 that the composite spectra of HRLQs in the different redshift bins match very well, especially in the sense that all of them show comparably strong emission lines. In Fig. 6, we also show the composite median spectrum of quasars that are detected in the FIRST survey and have $f_{1.4 \text{ GHz}} \geq 2 \text{ mJy}$ for comparison (Kimball et al. 2011a).

The histograms of $\Delta\alpha_{\text{ox,RQQ}}$ and $\Delta\alpha_{\text{ox,RLQ}}$ for the two samples are shown in Fig. 7, where the low- z sample contains upper limits as some HRLQs from Miller11 were not detected in X-rays. The distributions for the high- z and low- z samples are visually different, with not only their peaks differing by ≈ 0.1 , but also their distributions spanning different

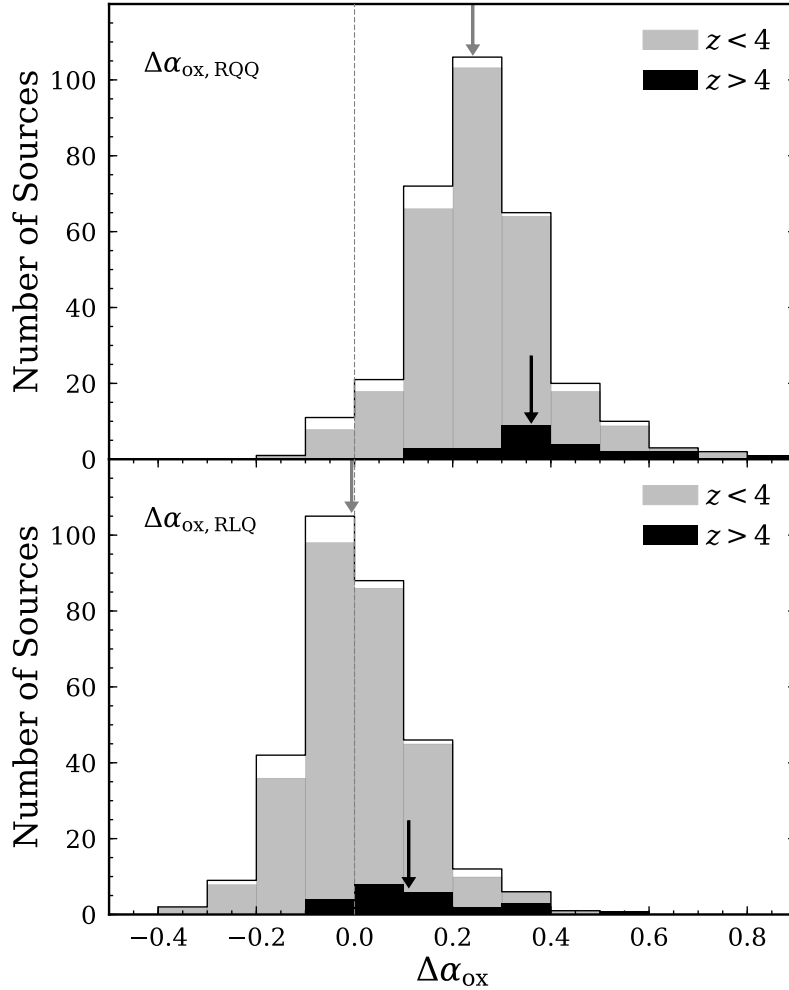


Figure 7. The histograms of $\Delta\alpha_{\text{ox,RQQ}}$ (top) and $\Delta\alpha_{\text{ox,RLQ}}$ (bottom) for the full-sample objects in Miller11 with $\log R > 2.5$, $z < 4$, and $m_i \leq 20.26$. The gray and open histograms are for X-ray detected and undetected objects in the $z < 4$ sample, respectively. The HRLQs at $z > 4$ are plotted in black. The downward arrows indicate the medians of the $\Delta\alpha_{\text{ox}}$ distributions of the two redshift bins.

ranges, in both panels. From the histograms of $\Delta\alpha_{\text{ox,RLQ}}$, the HRLQs at $z < 4$ do not show an apparent deviation from the $L_2 \text{ keV} - L_{2500 \text{ \AA}} - L_5 \text{ GHz}$ relation that is derived from their parent population of general RLQs. However, HRLQs at $z > 4$ do not follow this relation well and have an excess of X-ray emission compared with the low-redshift sample.

4.2 Quantitative statistical tests

Since there are upper limits²¹ in our comparison sample, to quantify the statistical significance of the difference in the $\Delta\alpha_{\text{ox}}$ distributions of the two samples, we use the Peto-Prentice test that is implemented in the Astronomy Survival Analysis Package²² to perform two-sample tests. The

²¹ Note that Miller11 calculated relatively conservative 95% confidence upper limits for the X-ray flux when a quasar is not detected in X-rays. Considering the 19 non-detections in the low- z sample, ≈ 18 are expected to be correct in the sense that the flux is actually below the limit value.

²² Downloaded from <http://astrostatistics.psu.edu/statcodes/asurv>. See Feigelson & Nelson (1985).

test shows a 4.56σ ($p = 2.56 \times 10^{-6}$)²³ difference for the $\Delta\alpha_{\text{ox,RQQ}}$ distributions and a 4.07σ ($p = 2.35 \times 10^{-5}$) difference for the $\Delta\alpha_{\text{ox,RLQ}}$ distributions, both of which are better than the corresponding statistical significances measured by Wu13. Furthermore, while the statistical test results of Wu13 should be considered as suggestive (due to their incomplete X-ray coverage), our results can be accepted more formally.

The majority of the high- z sample that has multi-frequency data in the radio band is flat-spectrum ($\alpha_r > -0.5$) objects (see Table 5). We thus performed another statistical test on the subsets of confirmed flat-spectrum quasars selected from the high- z and low- z samples. The differences of the high- z subset (17 objects) and low- z subset (100 objects) are 4.18σ ($p = 1.46 \times 10^{-5}$) and 3.18σ ($p = 7.36 \times 10^{-4}$) for the distributions of $\Delta\alpha_{\text{ox,RQQ}}$ and $\Delta\alpha_{\text{ox,RLQ}}$, respectively. We performed a Monte Carlo simulation by randomly selecting 17 and 100 objects from the flux-limited high- z (24 objects) and low- z (311 objects) samples and running statistical tests

²³ The p -values in this section are the probabilities of the data under the null hypothesis and correspond to the significance level in one-sided tests using a standard normal distribution.

on these sub-samples. The statistical significance typically drops by $\approx 1\sigma$ compared with that of the flux-limited sample; we conclude that the smaller statistical significance resulting from the flat-spectrum sub-sample is mainly caused by the smaller sample size, rather than any strong systematic difference in the degree of high- z enhancement.

Another factor that inevitably affects our statistical tests and all other such tests in the literature is the uncertainties of α_{ox} and $\Delta\alpha_{\text{ox}}$, including contributions from flux measurement errors and intrinsic quasar variability (since the multi-wavelength data have not been simultaneously obtained). The uncertainties of the X-ray fluxes are in the range of 6%–30% (e.g. see Table 3); the flux errors in the optical ($\sigma_{m_i} \lesssim 0.03$ mag) and radio ($\sigma_{\text{rms}} \lesssim 0.15$ mJy) are negligible compared with those for the X-rays. Since the overall variability (in X-rays and optical) dominates the uncertainties, we adopted a typical value of 20% for uncertainties due to flux errors in X-rays. We take a magnitude of 25% for the variability in the X-ray band (e.g. Gibson & Brandt 2012) and a magnitude of 25% for the variability in the optical/UV (considering our sample contains the most-luminous quasars and RLQs are usually more variable than RQQs, e.g. Vanden Berk et al. 2004; MacLeod et al. 2010). We thus assign a typical value of 0.06 as the uncertainties on α_{ox} , which is equivalent to $\approx 43\%$ uncertainties on the amount of X-ray enhancement. Both measurement errors and variability are random uncertainties instead of systematic biases, and they thus broaden the $\Delta\alpha_{\text{ox}}$ distributions with the centres unchanged. The Peto-Prentice tests we performed in the analyses above compare, in fact, the broadened distributions instead of the true distributions. One of the consequences is that the power of the statistical tests is reduced by the “smearing” effect of the uncertainties. In another words, if we had performed coordinated multi-wavelength observations using telescopes powerful enough to ignore the measurement errors, the statistical significance would be even higher. We confirmed the effects of the uncertainties on α_{ox} on two-sample tests using Monte Carlo simulations. We also confirmed the even higher statistical significance of the “true” distribution using Bayesian modelling, marginalising out the uncertainties of α_{ox} . See Appendix B for details on the simulation and modelling process. We note that the simulation can indicate the direction of the effects of uncertainties while we are not sure whether a quantitative correction to the statistical significance is well justified or not, and the modelling analysis depends on assumptions (e.g. the Gaussian assumption, the magnitudes of the uncertainties, and priors). We thus conservatively quote the results of the statistical tests using the observed data, following the standard practice in the literature.

Among the 7 objects (excluding SDSS J091316.55+591921.6) in Table 5 that are outside the flux-limited sample, three objects have less X-ray emission than predicted from the $L_{2\text{keV}}-L_{2500\text{\AA}}-L_{5\text{GHz}}$ relation of low- z RLQs (negative $\Delta\alpha_{\text{ox,RLQ}}$ values). In comparison, only four out of 24 objects in the flux-limited sample show this deficit of X-ray emission. Since our multi-wavelength data are not simultaneous, variability with larger amplitude for fainter objects may generally cause larger scatter of α_{ox} . We cannot conclude from the available data that the X-ray enhancement disappears in the optically faint regime. We will need complete X-ray coverage of optically fainter

HRLQs at $z > 4$ to improve understanding of this matter (see Section 5.3).

4.3 The amount of X-ray enhancement

We quantify the typical amount of X-ray enhancement for the high- z sample relative to the low- z sample using the difference of the medians of their $\Delta\alpha_{\text{ox}}$ distributions. The medians were calculated using the Kaplan-Meier estimator of the cumulative distribution function that can cope with upper limits in data. We describe the relevant methodology in Appendix C. The medians of $\Delta\alpha_{\text{ox,RQQ}}$ for the high-redshift and low-redshift samples are 0.37 ± 0.03 and 0.24 ± 0.01 , respectively. The medians of $\Delta\alpha_{\text{ox,RLQ}}$ for the high-redshift and low-redshift samples are 0.11 ± 0.03 and 0.01 ± 0.02 , respectively. The uncertainties here are estimated using bootstrapping (see the method in Appendix C). These medians are also plotted in Fig. 7 as downward arrows. The difference of the medians of the $\Delta\alpha_{\text{ox,RLQ}}$ distributions is 0.11 ± 0.04 , and thus the X-ray luminosities of the HRLQs at $z > 4$ are typically $1.9^{+0.5}_{-0.4}$ times those of their low-redshift counterparts. In addition to the median factor of X-ray enhancement, we also calculate the interquartile range from the $\Delta\alpha_{\text{ox,RLQ}}$ distribution of the high- z sample, which is $[0.04, 0.21]$ and corresponds to a factor of X-ray enhancement in the range of $[1.3, 3.5]$. At the extremes, some objects show no X-ray enhancement while others show an enhancement by a factor of 5–25 (see Table 5).

The factor of $1.9^{+0.5}_{-0.4}$ X-ray enhancement is somewhat smaller than but consistent with the estimation in Wu13, who found a factor of ≈ 3 by comparing the means of $\Delta\alpha_{\text{ox}}$. We thus calculate the factor of X-ray enhancement using the median statistic and the 12 HRLQs that were used by Wu13 ($m_i < 20$) resulting in a factor of $2.6^{+2.0}_{-1.0}$. Therefore, any apparent difference of X-ray enhancement factor is mainly caused by the large scatter due to the small sample size of Wu13 and partly by the statistic used.

We here point out one potential Malmquist-type bias (e.g. Lauer et al. 2007) that could diminish the X-ray enhancement of the high-redshift sample compared with the low-redshift sample. A larger fraction of the high- z sample is near the optical flux limit ($m_i = 20.26$) than the low- z sample; if the optical luminosity function is steep, a large fraction of the HRLQs that are near the flux limit have, intrinsically, a dim X-ray flux. We thus select another low- z HRLQ sample with $\log L_{2500\text{\AA}} > 30.57$, which is the minimum optical/UV luminosity of the high- z sample. The resulting low- z sample has a size of 165. We found that the X-ray enhancement of the high- z sample is a factor of $2.0^{+0.5}_{-0.4}$, which means this selection effect, if it exists, probably does not significantly affect our results.

4.4 HRLQs at $3 < z < 4$

Wu13 performed two-sample tests on HRLQs in different redshift bins below $z = 4$ using the RLQs of Miller11 and found an apparent X-ray enhancement also exists at $z \approx 3$. Specifically, the $\Delta\alpha_{\text{ox}}$ distributions of HRLQs at $3 < z < 4$ differ from those of $z < 3$ HRLQs at a $\approx 5\sigma$ level. We thus select $3 < z < 4$ HRLQs from the full RLQ sample and quantify their typical factor of X-ray enhancement relative

to HRLQs at $z < 3$ using the same consistent method described in the previous section. We have applied an optical flux cut determined by the faintest HRLQ at $3 < z < 4$ ($m_i = 20.38$). The sample sizes (median redshifts) are 16 ($z = 3.4$) and 304 ($z = 1.3$) for $3 < z < 4$ HRLQs and $z < 3$ HRLQs, respectively. We estimated the medians of $\Delta\alpha_{\text{ox,RLQ}}$ for $3 < z < 4$ and $z < 3$ objects are 0.12 ± 0.07 and -0.01 ± 0.01 . The corresponding factor of X-ray enhancement is $2.0^{+1.1}_{-0.8}$. The relatively larger error bars of our estimations are largely due to the small sample size at $3 < z < 4$.

4.5 The spectral energy distributions

We here make another comparison between the X-ray emission of high- z and low- z HRLQs using their SEDs. We collected photometric data to construct the broadband SEDs of our objects that cover the radio through X-ray bands from the following sources.

(i) Radio: the 1.4 GHz flux densities are from the FIRST or NVSS surveys; the sources for 5 GHz values are the same as those described in Column (12) in Section 3.5; the 150 MHz flux densities are gathered from the GMRT 150 MHz all-sky survey (Intema et al. 2017); the flux densities at other frequencies were retrieved from the NED.

(ii) Mid-infrared: the all-sky catalog of the *Wide-field Infrared Survey Explorer* (WISE; Wright et al. 2010) provides the mid-infrared fluxes. All of our objects are detected by WISE except for SDSS J083549.42+182520.0, SDSS J102107.57+220921.4, and SDSS J160528.21+272854.4.

(iii) Near-infrared: we first searched for objects in the Two Micron All Sky Survey (2MASS; Skrutskie et al. 2006). None of our objects has a 2MASS detection. We then searched objects in the UKIRT Infrared Deep Sky Survey (UKIDSS; Lawrence et al. 2007). Five objects (SDSS J030437.21+004653.5, PMN J2314+0201, SDSS J083549.42+182520.0, SDSS J153533.88+025423.3, and SDSS J222032.50+002537.5) have Y , J , H , and K detections, while SDSS J160528.21+272854.4 has only a J -band detection. We further searched for objects in the VISTA Hemisphere Survey (VHS; McMahan et al. 2013), where we found J -, H -, and K_s -band detections for SDSS J030437.21+004653.5, PMN J2134-0419, and SDSS J222032.50+002537.5, and an additional Y -band detection for PMN J2134-0419.

(iv) Optical: obtained from SDSS photometry (u , g , r , i , and z). The bands that are seriously affected by the Ly α forest are discarded.

(v) X-ray: from this work.

None of our HRLQs has a counterpart in the *Fermi* LAT 4-Year Point Source Catalog (Acero et al. 2015), using a matching radius of $10'$. The constructed SEDs of our HRLQs are shown in Fig 8, in ascending order of RA. Also plotted in Fig 8 is a comparison SED (grey curve) that was constructed by Wu13, using 10 HRLQs at $z < 1.4$ from Shang et al. (2011). These 10 low- z HRLQs were selected based on their optical/UV luminosity ($\log \lambda L_\lambda(3000\text{\AA}) > 45.9$), radio-loudness ($2.9 < \log R < 3.7$), and useful X-ray data from the literature. Their SEDs were normalised at rest-frame 4215 \AA , and medians for different waveband bins were calculated (see Section 5.2 of Shang et al. 2011). Following Wu13, we have

normalised the comparison SED to the observed data for our HRLQs at rest-frame 2500 \AA .

Five out of the 15 HRLQs have higher X-ray luminosities by a factor of ≈ 3 –13 than that of the comparison SED, while the other 10 HRLQs have comparable X-ray luminosities with that of the comparison SED, considering the uncertainties of the X-ray luminosities. Note that the interquartile ranges of the comparison SED are 0.37 dex and 0.56 dex in the radio (5 GHz) and X-ray (2 keV) bands, respectively. Notably, SDSS J102107.57+220921.4 and SDSS J083549.42+182520.0 show a factor of ≈ 10 enhancement in their X-ray luminosities relative to the comparison SED; both of them were not included in our flux-limited sample due to their fainter optical fluxes, making future work that extends our systematic study to the fainter optical regime promising (see Section 5.3). Including the 17 SEDs of Wu13, half of the high- z HRLQs (16/32) show an apparent excess of X-ray emission by a factor of ~ 2.5 –20, compared with the low- z HRLQs with matched optical/UV luminosity and radio-loudness. Also from their SEDs, the HRLQs do not show weaker optical/UV emission, relative to their infrared emission, which means the high $\Delta\alpha_{\text{ox}}$ values indeed reflect stronger X-ray emission instead of weaker optical/UV emission. This supports the basic validity of our earlier analyses based on $\Delta\alpha_{\text{ox}}$.

5 SUMMARY, DISCUSSION, AND FUTURE WORK

5.1 Summary

In this paper, we have tested and confirmed the X-ray enhancement of high-redshift ($z > 4$) HRLQs ($\log R > 2.5$) compared with their low-redshift ($z < 4$) counterparts. We summarize the key points from this work:

(i) We selected the high-redshift ($z > 4$) HRLQs from Wu13 and new objects from sky surveys (SDSS and FIRST) and NED. We obtained *Chandra* observations in Cycle 17 for 6 HRLQs that lacked sensitive X-ray coverage. We also retrieved archival *XMM-Newton* and *Swift* X-ray observations that cover another nine high- z HRLQs. We finally constructed an optically flux-limited sample of 24 HRLQs to $m_i = 20.26$ that has complete sensitive X-ray coverage. See Section 2.

(ii) We analyzed the X-ray data and measured HRLQ X-ray photometric properties (see Table 3). All the *Chandra* Cycle 17 objects were detected in X-rays. No extended structure was found in the *Chandra* images, including for SDSS J0813+3508, which is the only *Chandra* Cycle 17 object that has an extended structure in its FIRST image. See Section 3.

(iii) HRLQs at $z > 4$ show an apparent X-ray enhancement compared with matched HRLQs at $z < 4$. The $\Delta\alpha_{\text{ox}}$ (including $\Delta\alpha_{\text{ox,RQQ}}$ and $\Delta\alpha_{\text{ox,RLQ}}$) distributions of the optically flux-limited high- z sample are significantly different (≈ 4 – 4.6σ) from those of the low- z sample. This result confirms the relevant result of Wu13, in a statistically stronger way and with fewer systematic uncertainties. See Section 4.2.

(iv) The typical (median) X-ray enhancement of HRLQs at $z > 4$ is a factor of $1.9^{+0.5}_{-0.4}$; this is smaller than but still consistent with the estimation of Wu13. See Section 4.3.

(v) We constructed the radio–X-ray continuum SEDs for

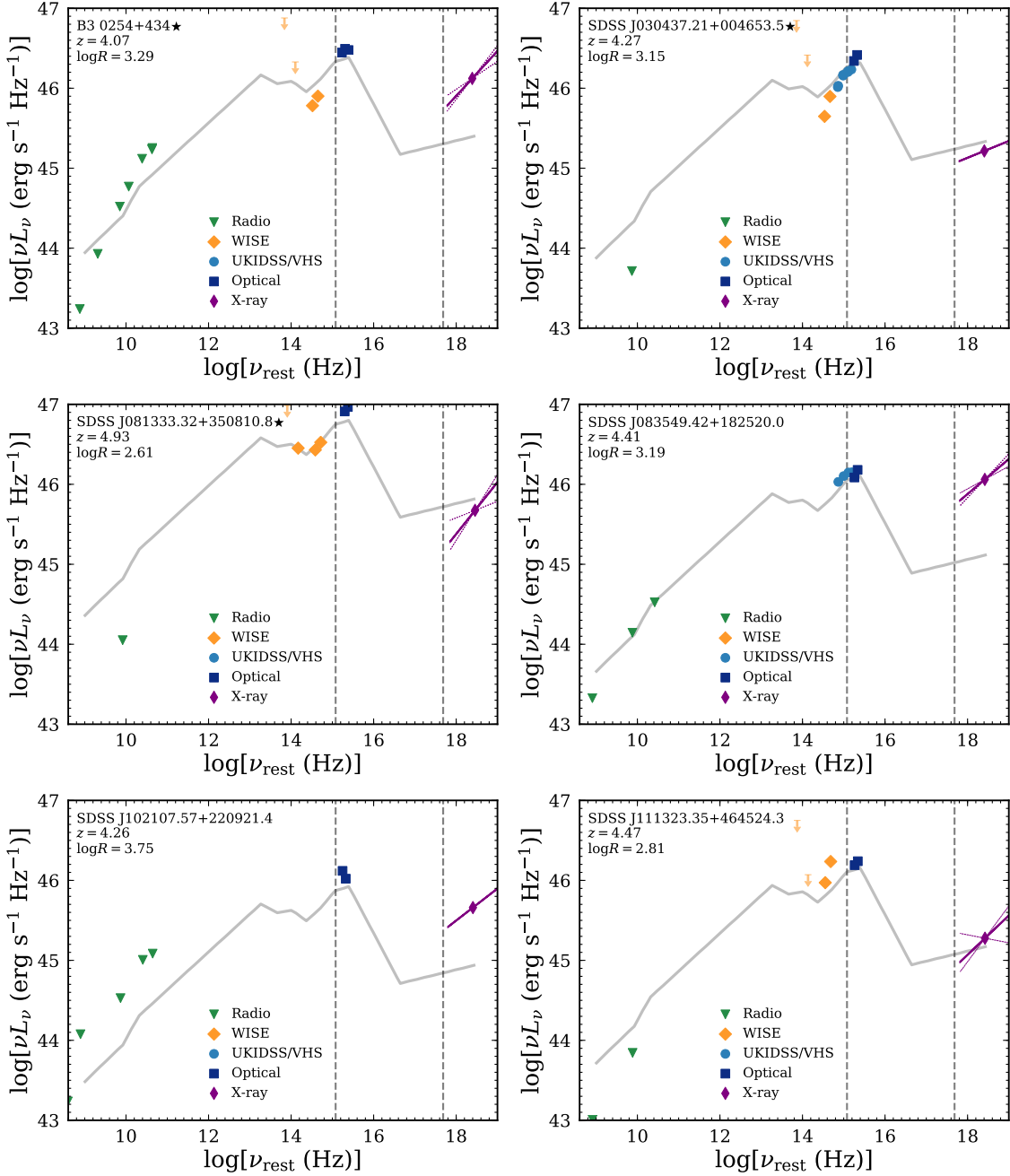


Figure 8. The broadband SEDs for the HRLQs in this paper (in ascending order of RA) from radio to X-ray. The objects within our flux-limited sample are marked by \star following their names. The solid purple lines show the X-ray power-law spectra with their uncertainties as dotted lines (see Column (9) in Section 3.5). The purple diamonds represent the observed-frame 2 keV. The grey curve is the composite SED for the 10 HRLQs at $z < 1.4$ from Shang et al. (2011) with comparable optical luminosity and radio loudness. This low- z comparison SED has been normalised to the high- z SEDs at rest-frame 2500 Å. The vertical lines indicate rest-frame 2500 Å and 2 keV.

the HRLQs analyzed in this paper, which further illustrate and support the excess of X-ray emission of high- z HRLQs compared with their low- z counterparts. See Section 4.5.

5.2 Discussion

We have confirmed the X-ray enhancement of HRLQs at $z > 4$ that was originally proposed by Wu13. However, we

revised the typical amount of X-ray enhancement from a factor of ≈ 3 to ≈ 2 . We plot the factor of X-ray enhancement using the estimates for HRLQs at $z > 4$ in Fig. 9. The fractional IC/CMB model that was suggested by Wu13 can still explain our results if the fraction of X-rays from the IC/CMB mechanism in HRLQs decreases accordingly. More specifically, if IC/CMB produces 3% of the X-ray radiation from HRLQs at $z = 1.3$, a factor of ≈ 2 X-ray enhancement at our median redshift of $z = 4.4$ can be reproduced accord-

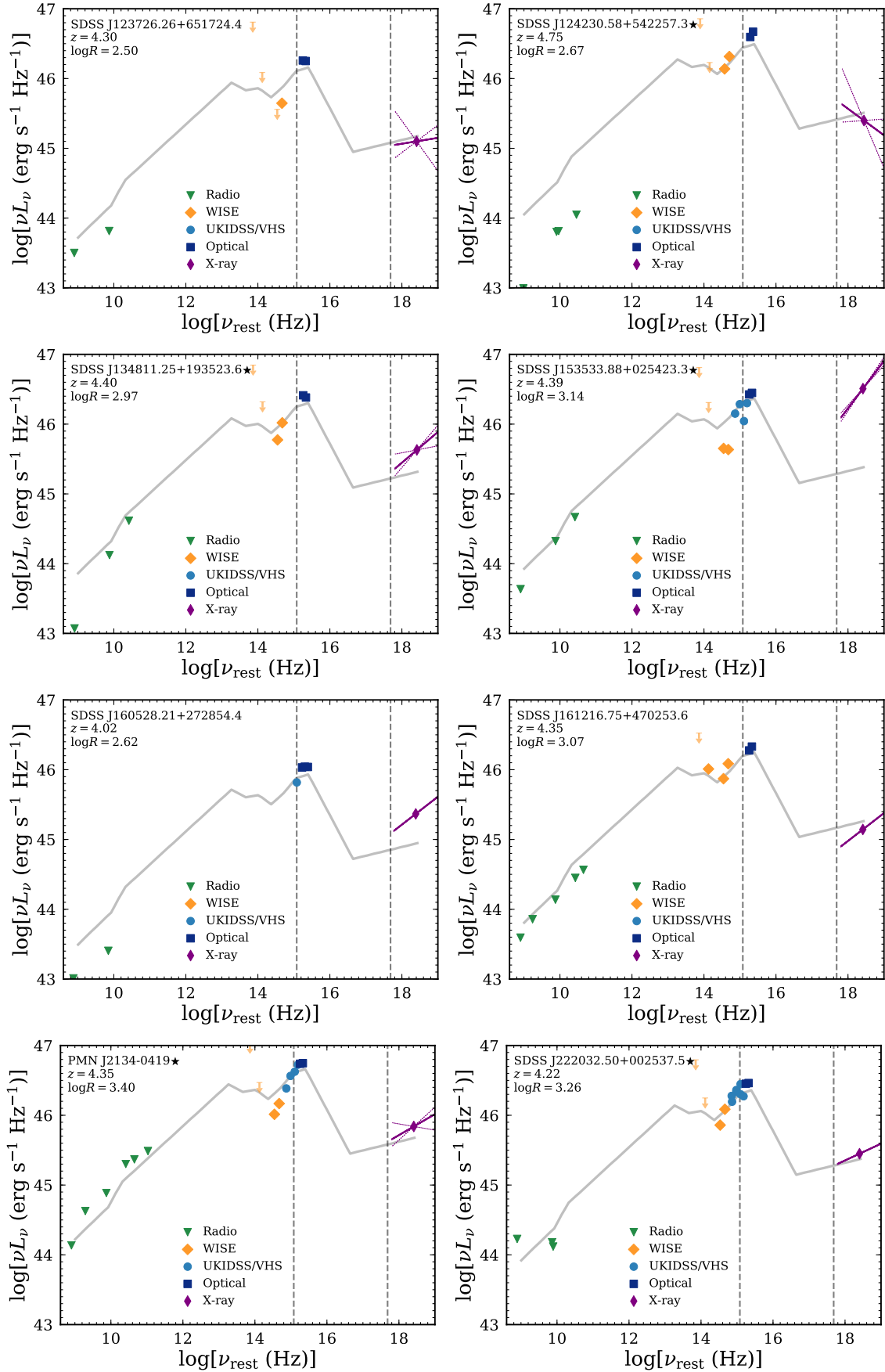


Figure 8 (Continued).

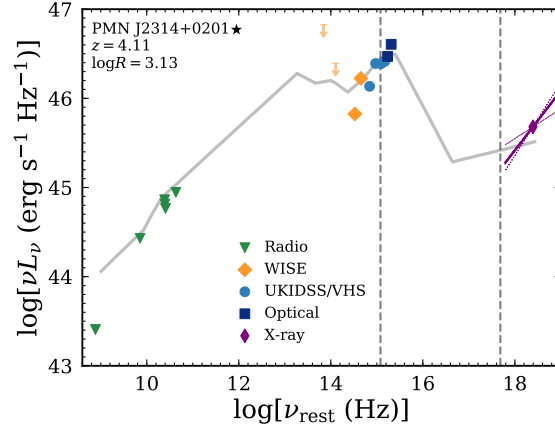


Figure 8 (Continued).

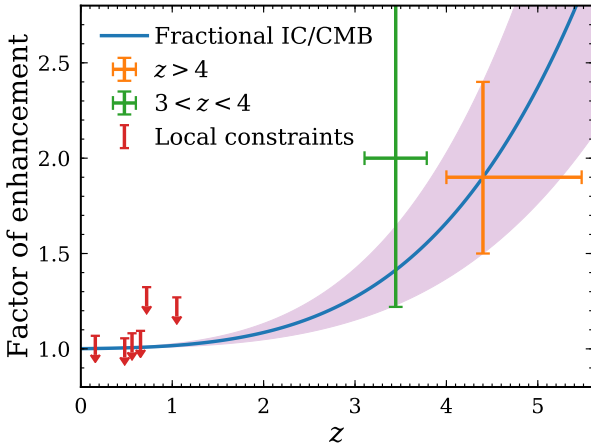


Figure 9. The current constraints on the evolution of the X-ray enhancement of HRLQs using the $z > 4$ sample from this paper and Wu13 and the $3 < z < 4$ sample from Miller11. The blue curve and purple-shaded region are the prediction from the fractional IC/CMB model and its uncertainties, which are calibrated using the $z > 4$ redshift bin. We constrain the contribution of the IC/CMB mechanism at $z = 1.3$ to be $\approx 3\%$, with an upper limit of $\approx 5\%$. The red upper limits are the constraints from non-detections of IC/CMB-predicted γ -ray emission from low- z large-scale jets using *Fermi* (Meyer et al. 2015; Breiding et al. 2017; Meyer et al. 2017). See Section 5.2 for details.

ing to $U_{\text{CMB}} \propto (1+z)^4$ evolution, assuming that the high- z jets are not physically different (e.g. severely decelerated on kpc scales; Lopez et al. 2006; Volonteri et al. 2011; Marshall et al. 2018) from the low- z jets.

We have plotted in Fig. 9 the prediction and uncertainties of our revised fractional IC/CMB model for the factor of X-ray enhancement with redshift (blue curve and purple-shaded region). The curve has the form of $1 + A[(1+z)/(1+4.4)]^4$, which represents the combination of a non-evolving component and an evolving IC/CMB-related component. This curve is calibrated by the analysis of $z > 4$ HRLQs. For example, A needs to be ≈ 0.9 for the blue curve to match the observed enhancement of 1.9 at $z = 4.4$. The boundary of the shaded region is determined accordingly using the error bars of the $z = 4.4$ data point. The curve is consistent

with the constraint from $3 < z < 4$ HRLQs, which show more substantial uncertainties due to limited sample size. A larger sample will help to provide tighter constraints on the X-ray enhancement of HRLQs in this redshift bin. Note that at $z \approx 1$ and $z \approx 2$ the expected X-ray enhancements are only factors of 1.02 and 1.09, with upper limits of 1.03 and 1.13, respectively.

Recall that the quasars with high-resolution *Chandra* observations in our sample do not show any extended structure in their X-ray images, and the jet-linked X-ray emission is most probably from regions smaller than a few kpc. The high- z large-scale X-ray jets (if they exist) must lie below the flux limits of our X-ray observations and are much dimmer than the core region, in contrast with the prediction of the most-straightforward IC/CMB model under the assumption that the radio fluxes of the jets relative to those of the cores do not evolve with redshift (Schwartz 2002; also see Bassett et al. 2004; Lopez et al. 2006; Miller11). Either a high-energy synchrotron-emitting electron population or an improved understanding of quasar jets is needed to explain the commonly detected large-scale X-ray jets of low- z quasars.

The IC/CMB-dominated model for the X-ray emission of large-scale quasar jets predicts significant radiation in the high-energy γ -ray band (e.g. Tavecchio et al. 2004), and *Fermi* observations have thus been suggested to be used to test the IC/CMB model (e.g. Dermer & Atoyan 2004). The first such test was performed by Meyer & Georganopoulos (2014) on the large-scale jet of 3C 273 and their results disfavoured the IC/CMB-dominated model. We here compare the constraints on the IC/CMB X-ray emission from our high- z quasars with the constraints from $z \approx 0.1$ –1 large-scale jets, which are shown as upper limits in Fig. 9. The six upper limits are the following: 1.068 (3C 273, $z = 0.160$; Meyer et al. 2015), 1.095 (PKS 0637–752, $z = 0.650$; Meyer et al. 2017), 1.055 (PKS 2209+080, $z = 0.480$), 1.082 (PKS 1136–135, $z = 0.560$), 1.324 (PKS 1354+195, $z = 0.720$), and 1.269 (PKS 1229–021, $z = 1.05$; Breiding et al. 2017). Following Meyer et al. (2015), we have assumed the “angle-averaged” jet-linked X-ray emission from those low- z RLQs is dominated by large-scale jets, after correcting for the beaming effect of the radiation from the cores. We calculated the ratio between the upper limit from the *Fermi* data and the

predicted IC/CMB γ -rays, which is equivalent to the upper limit on the fraction of IC/CMB X-ray emission to total jet-linked X-rays. Since the literature has divided the *Fermi* bandpass into multiple sub-bands, we have chosen the band giving the most-stringent constraint.

Note that early X-ray studies using representative samples of moderately radio-loud to highly radio-loud ($1 \lesssim \log R \lesssim 4$) quasars at $z > 4$ (e.g. Bassett et al. 2004; Lopez et al. 2006; Wu13) have argued against the scenario where the IC/CMB mechanism plays a dominant role in the jet-linked X-ray emission from these high-redshift objects (e.g. Schwartz 2002). In addition, Miller11 found no evidence supporting an apparent redshift dependence of X-ray properties in their large-sample (607 objects) study of RLQs that spans $0 < z < 5$ and $1 < \log R < 5$.

Indeed, considering the X-ray jets of PKS 0637–752 ($z = 0.650$, $L_{2-10 \text{ keV}} \approx 4 \times 10^{44} \text{ erg s}^{-1}$; Schwartz et al. 2000) and B3 0727+409 ($z = 2.5$, $L_{2-10 \text{ keV}} \approx 6 \times 10^{44} \text{ erg s}^{-1}$; Simionescu et al. 2016), if the IC/CMB model were responsible for their X-ray emission, their analogs at $z \approx 4.4$ would have $L_{2-10 \text{ keV}} \approx 5 \times 10^{46} \text{ erg s}^{-1}$ and $L_{2-10 \text{ keV}} \approx 3 \times 10^{45} \text{ erg s}^{-1}$, both of which would outshine their cores in X-rays. However, X-ray observations of RLQs at $z > 4$ do not support this prediction (e.g. Bassett et al. 2004; Lopez et al. 2006; Saez et al. 2011; Miller et al. 2011; Wu13).²⁴ Note that the X-ray luminosities of the few resolved $z > 4$ kpc-scale jets are only a few percent that of the quasar cores (e.g. Yuan et al. 2003; Cheung et al. 2012), consistent with the results for low- z jets.

McKeough et al. (2016) investigated the redshift dependence of the X-ray-to-radio flux ratios (α_{XR}) of 11 quasars and found that the $z > 3$ quasars have marginally stronger X-ray emission relative to the $z < 3$ quasars in their sample. Marshall et al. (2018) studied the α_{RX} distribution of 56 quasar jets at $z \lesssim 2$ and found weak redshift dependence with their $0.95 < z < 2.05$ sub-sample showing marginally larger X-ray flux densities relative to that of radio than their $0.55 < z < 0.95$ sub-sample. Their results disfavour the scenario where the IC/CMB mechanism dominates the jets' X-ray emission (without changing the properties of high- z jets) and are consistent with our previous result from $z > 4$ RLQs.

Wu13 also discussed another possible cause of the X-ray enhancements in which the photon field of the host galaxy inverse-Compton scatters off the relativistic electrons in the jets. This mechanism requires the host galaxies at high redshifts to have enhanced star-formation activity that produces dense infrared photon fields (e.g. Wang et al. 2011; Mor et al. 2012; Netzer et al. 2014). Our results can still be explained by this scenario. While the cosmological evolution of the CMB energy density can be easily predicted, the evolution of the star-forming activity of the hosts of quasars with powerful relativistic jets at different redshifts has not been established (e.g. Archibald et al. 2001). However, if future X-ray studies of HRLQs that extend to $z \approx$

0.5–4 detect any deviation from the prediction of the blue curve in Fig. 9 and disfavour the fractional IC/CMB model, alternative models like this will gain more credit.

Ajello et al. (2009) found that the number density of flat-spectrum radio quasars (FSRQs) selected by the *Swift*/Burst Alert Telescope (BAT; in hard X-rays) has a peak at a notably high redshift of $z \approx 3$ –4. The interpretation of such a number-density peak can be affected by the X-ray luminosity enhancement of HRLQs at $z > 4$ we confirmed here. Qualitatively, this X-ray enhancement might cause high- z HRLQs to be more easily picked up by *Swift*/BAT, and their apparent peak in number density will correspondingly be biased toward a higher redshift. A quantitative discussion of this issue is beyond the scope of this paper.

5.3 Future work

There are several ways the results in this work might be productively extended. First, the sample statistics of the $z > 4$ HRLQs could be improved by future X-ray observations of the additional objects listed in Table 2. Several objects in Table 2 have already been scheduled for *Chandra* observations, and a *Chandra* snapshot survey of the remaining objects would extend complete X-ray coverage to an optically flux-limited sample reaching $m_i = 21$ with a size of 37. With this larger sample size, the level of X-ray enhancement of $z > 4$ HRLQs could be better constrained.

Furthermore, one could now substantially enlarge the sample of HRLQs at $z < 4$ with sensitive X-ray coverage via systematic archival data mining. The Miller11 sample used for our $z < 4$ comparisons here was largely based on SDSS Data Release 5 (DR5) from 2007 (e.g. Schneider et al. 2007), and it utilized X-ray coverage from *Chandra*, *XMM-Newton*, and *ROSAT*. Over the past decade, more than 450,000 new quasars have been spectroscopically identified by the SDSS (e.g. P aris et al. 2018), including many new HRLQs at $z \approx 0.5$ –4. Furthermore, the sizes of the *Chandra* and *XMM-Newton* archives have grown substantially since the work of Miller11, and more sensitive radio data have been gathered in the SDSS footprint (e.g. via the ongoing VLA Sky Survey²⁵). Systematic archival X-ray analyses of these new $z \approx 0.5$ –4 HRLQs should allow more precise measurements of the factor of X-ray enhancement vs. redshift (see Figure 9), thereby testing and quantifying the fractional IC/CMB model.

Finally, alternative explanations of the observed X-ray enhancement should also be explored. For example, ALMA measurements of star-formation rates for $z > 4$ HRLQ hosts could test if their star formation is sufficiently elevated to drive the X-ray enhancement via a stronger host seed photon field (see Section 1).

ACKNOWLEDGEMENTS

We thank M. Ajello, D. P. Schneider, and W. M. Yi for helpful discussions. We thank the referee for helpful comments. SFZ and WNB acknowledge support from the Penn State

²⁴ B3 0727+409 has a large-scale jet that is bright at X-ray and faint at radio, which is thought to be consistent with the prediction of IC/CMB model (Simionescu et al. 2016). However, B3 0727+409 has a core that is extremely radio-loud ($\log R \approx 6$), and thus its analog at $z > 4$ will not be missed by our selection criterion.

²⁵ <https://science.nrao.edu/science/surveys/vlass>

ACIS Instrument Team Contract SV4-74018 (issued by the *Chandra* X-ray Center, which is operated by the Smithsonian Astrophysical Observatory for and on behalf of NASA under contract NAS8-03060) and CXC grant AR8-19011X. The *Chandra* Guaranteed Time Observations (GTO) for some of the quasars studied herein were selected by the ACIS Instrument Principal Investigator, Gordon P. Garmire, currently of the Huntingdon Institute for X-ray Astronomy, LLC, which is under contract to the Smithsonian Astrophysical Observatory via Contract SV2-82024.

REFERENCES

- Acerro, F., Ackermann, M., Ajello, M., et al. 2015, *ApJS*, 218, 23
- Ajello, M., Costamante, L., Sambruna, R. M., et al. 2009, *ApJ*, 699, 603
- Amirkhanyan, V. R. & Mikhailov, V. P. 2006, *Astrophysics*, 49, 184
- Archibald, E. N., Dunlop, J. S., Hughes, D. H., et al. 2001, *MNRAS*, 323, 417
- Atoyan, A. & Dermer, C. D. 2004, *ApJ*, 613, 151
- Avni, Y., Soltan, A., Tananbaum, H., & Zamorani, G. 1980, *ApJ*, 238, 800
- Bassett, L. C., Brandt, W. N., Schneider, D. P., et al. 2004, *AJ*, 128, 523
- Becker, R. H., White, R. L., & Helfand, D. J. 1995, *ApJ*, 450, 559
- Begelman, M. C., Blandford, R. D. & Rees, M. J. 1984, *Reviews of Modern Physics*, 56, 255
- Brandt, W. N., & Alexander, D. M. 2015, *A&ARv*, 23, 1
- Brandt, W. N., Schneider, D. P., Fan, X., et al. 2002, *ApJ*, 569, L5
- Breiding, P., Meyer, E. T., Georganopoulos, M., et al. 2017, *ApJ*, 849, 95
- Brunetti, G., Comastri, A., Setti, G., et al. 1999, *A&A*, 342, 57
- Burrows, D. N., Hill, J. E., Nousek, J. A., et al. 2005, *Space Sci. Rev.*, 120, 165
- Cao, H.-M., Frey, S., Gabányi, K. É., et al. 2017, *MNRAS*, 467, 950
- Celotti, A., Ghisellini, G., & Chiaberge, M. 2001, *MNRAS*, 321, L1
- Chartas, G., Worrall, D. M., Birkinshaw, M., et al. 2000, *ApJ*, 542, 655
- Cheung, C. C., Stawarz, L., Siemiginowska, A., et al. 2012, *ApJ*, 756, L20
- Conrad, J. 2015, *Astroparticle Physics*, 62, 165
- Condon, J. J., Cotton, W. D., Greisen, E. W., et al. 1998, *AJ*, 115, 1693
- Dermer, C. D. & Atoyan, A. 2004, *ApJ*, 611, L9
- Dickey, J. M., & Lockman, F. J. 1990, *ARA&A*, 28, 215
- Fan, X. 2012, *Research in Astronomy and Astrophysics*, 12, 865
- Feigelson, E. D., Laurent-Muehleisen, S. A., Kollgaard, R. I., et al. 1995, *ApJ*, 449, L149
- Feigelson, E. D., & Nelson, P. I. 1985, *ApJ*, 293, 192
- Felten, J. E. & Morrison, P. 1966, *ApJ*, 146, 686
- Freeman, P. E., Kashyap, V., Rosner, R., & Lamb, D. Q. 2002, *ApJS*, 138, 185
- Frey, S., Paragi, Z., Gurvits, L. I., Cseh, D., & Gabányi, K. É. 2010, *A&A*, 524, A83
- Hook, I. M., McMahon, R. G., Shaver, P. A., et al. 2002, *A&A*, 391, 509
- Garmire, G. P., Bautz, M. W., Ford, P. G., Nousek, J. A., & Ricker, G. R., Jr. 2003, *Proc. SPIE*, 4851, 28
- Ghisellini, G., & Tavecchio, F. 2009, *MNRAS*, 397, 985
- Gibson, R. R. & Brandt, W. N. 2012, *ApJ*, 746, 54
- Gibson, R. R., Brandt, W. N., & Schneider, D. P. 2008, *ApJ*, 685, 773
- Gregory, P. C., Scott, W. K., Douglas, K., & Condon, J. J. 1996, *ApJS*, 103, 427
- Hardcastle, M. J., & Croston, J. H. 2011, *MNRAS*, 415, 133
- Hardcastle, M. J. 2006, *MNRAS*, 366, 1465
- Harris, D. E. & Grindlay, J. E. 1979, *MNRAS*, 188, 25
- Harris, D. E., & Krawczynski, H. 2002, *ApJ*, 565, 244
- Harris, D. E., & Krawczynski, H. 2006, *ARA&A*, 44, 463
- Hewett, P. C., & Wild, V. 2010, *MNRAS*, 405, 2302
- Hodge, J. A., Becker, R. H., White, R. L., et al. 2011, *AJ*, 142, 3
- Hogan, B. S., Lister, M. L., Kharb, P., et al. 2011, *ApJ*, 730, 92
- Intema, H. T., Jagannathan, P., Mooley, K. P., et al. 2017, *A&A*, 598, A78
- Ivezić, Ž., Menou, K., Knapp, G. R., et al. 2002, *AJ*, 124, 2364
- Ivezić, Z., Richards, G., Hall, P., et al. 2004, *AGN Physics with the Sloan Digital Sky Survey*, 311, 347
- Jiang, L., Fan, X., Hines, D. C., et al. 2006, *AJ*, 132, 2127
- Just, D. W., Brandt, W. N., Shemmer, O., et al. 2007, *ApJ*, 665, 1004
- Kaplan, E. L., & Meier, P. 1958, *J. Amer. Statist. Assn.*, 53, 457
- Kataoka, J. & Stawarz, L. 2005, *ApJ*, 622, 797
- Kellermann, K. I., Sramek, R., Schmidt, M., Shaffer, D. B., & Green, R. 1989, *AJ*, 98, 1195
- Kelly, B. C. 2007, *ApJ*, 665, 1489
- Kimball, A. E., Ivezić, Ž., Wiita, P. J., et al. 2011a, *AJ*, 141, 182.
- Kimball, A. E., Kellermann, K. I., Condon, J. J., Ivezić, Ž., & Perley, R. A. 2011b, *ApJ*, 739, L29
- Kraft, R. P., Burrows, D. N., & Nousek, J. A. 1991, *ApJ*, 374, 344
- Lauer, T. R., Tremaine, S., Richstone, D., & Faber, S. M. 2007, *ApJ*, 670, 249
- Lawrence, A., Warren, S. J., Almaini, O., et al. 2007, *MNRAS*, 379, 1599
- Lopez, L. A., Brandt, W. N., Vignali, C., et al. 2006, *AJ*, 131, 1914
- Lu, Y., Wang, T., Zhou, H., et al. 2007, *AJ*, 133, 1615
- Lynden-Bell, D. 1971, *MNRAS*, 155, 95
- MacLeod, C. L., Ivezić, Ž., Kochanek, C. S., et al. 2010, *ApJ*, 721, 1014
- Marshall, H. L., Schwartz, D. A., Lovell, J. E. J., et al. 2005, *ApJS*, 156, 13
- Marshall, H. L., Gelbord, J. M., Worrall, D. M., et al. 2018, *ApJ*, 856, 66
- McGreer, I. D., Jiang, L., Fan, X., et al. 2013, *ApJ*, 768, 105
- McKeough, K., Siemiginowska, A., Cheung, C. C., et al. 2016, *ApJ*, 833, 123
- McMahon, R. G., Banerji, M., Gonzalez, E., et al. 2013, *The Messenger*, 154, 35
- Meyer, E. T. & Georganopoulos, M. 2014, *ApJ*, 780, L27
- Meyer, E. T., Georganopoulos, M., Sparks, W. B., et al. 2015, *ApJ*, 805, 154
- Meyer, E. T., Sparks, W. B., Georganopoulos, M., et al. 2016, *ApJ*, 818, 195
- Meyer, E. T., Breiding, P., Georganopoulos, M., et al. 2017, *ApJ*, 835, L35
- Miller, B. P., Brandt, W. N., Schneider, D. P., et al. 2011, *ApJ*, 726, 20 (Miller11)
- Mor, R., Netzer, H., Trakhtenbrot, B., Shemmer, O., & Lira, P. 2012, *ApJ*, 749, L25
- Mullin, L. M., & Hardcastle, M. J. 2009, *MNRAS*, 398, 1989
- Nanni, R., Vignali, C., Gilli, R., Moretti, A., & Brandt, W. N. 2017, *A&A*, 603, A128
- Netzer, H., Mor, R., Trakhtenbrot, B., Shemmer, O., & Lira, P. 2014, *ApJ*, 791, 34
- Padovani, P. 2017, *Nature Astronomy*, 1, 194
- Page, K. L., Reeves, J. N., O'Brien, P. T., & Turner, M. J. L. 2005, *MNRAS*, 364, 195
- Planck Collaboration, Ade, P. A. R., Aghanim, N., et al. 2016, *A&A*, 594, A13

Pâris, I., Petitjean, P., Aubourg, É., et al. 2018, *A&A*, 613, A51
 Park, T., Kashyap, V. L., Siemiginowska, A., et al. 2006, *ApJ*, 652, 610
 Richards, G. T., Strauss, M. A., Fan, X., et al. 2006, *AJ*, 131, 2766
 Rosen, S. R., Webb, N. A., Watson, M. G., et al. 2016, *A&A*, 590, A1
 Sæz, C., Brandt, W. N., Shemmer, O., et al. 2011, *ApJ*, 738, 53
 Sbarrato, T., Ghisellini, G., Tagliaferri, G., et al. 2015, *MNRAS*, 446, 2483
 Shang, Z., Brotherton, M. S., Wills, B. J., et al. 2011, *ApJS*, 196, 2
 Siemiginowska, A., Smith, R. K., Aldcroft, T. L., et al. 2003, *ApJ*, 598, L15
 Sikora, M., Stawarz, L., & Lasota, J.-P. 2007, *ApJ*, 658, 815
 Simionescu, A., Stawarz, L., Ichinohe, Y., et al. 2016, *ApJ*, 816, L15
 Singal, J., Petrosian, V., Stawarz, L., & Lawrence, A. 2013, *ApJ*, 764, 43
 Schmidt, M. 1968, *ApJ*, 151, 393
 Schmitt, J. H. M. M. 1985, *ApJ*, 293, 178
 Schneider, D. P., Hall, P. B., Richards, G. T., et al. 2007, *AJ*, 134, 102
 Schneider, D. P., Richards, G. T., Hall, P. B., et al. 2010, *AJ*, 139, 2360
 Schwartz, D. A., Marshall, H. L., Lovell, J. E. J., et al. 2000, *ApJ*, 540, 69
 Schwartz, D. A. 2002, *ApJ*, 569, L23
 Schlafly, E. F., & Finkbeiner, D. P. 2011, *ApJ*, 737, 103
 Shemmer, O., Brandt, W. N., Paolillo, M., et al. 2017, *ApJ*, 848, 46
 Shemmer, O., Brandt, W. N., Schneider, D. P., et al. 2006, *ApJ*, 644, 86
 Shen, Y., Richards, G. T., Strauss, M. A., et al. 2011, *ApJS*, 194, 45
 Skrutskie, M. F., Cutri, R. M., Stiening, R., et al. 2006, *AJ*, 131, 1163
 Spergel, D. N., Verde, L., Peiris, H. V., et al. 2003, *ApJS*, 148, 175
 Stark, A. A., Gammie, C. F., Wilson, R. W., et al. 1992, *ApJS*, 79, 77
 Strüder, L., Briel, U., Dennerl, K., et al. 2001, *A&A*, 365, L18
 Sambruna, R. M., Gambill, J. K., Maraschi, L., et al. 2004, *ApJ*, 608, 698
 Tananbaum, H., Avni, Y., Branduardi, G., et al. 1979, *ApJ*, 234, L9
 Tavecchio, F., Maraschi, L., Sambruna, R. M., & Urry, C. M. 2000, *ApJ*, 544, L23
 Tavecchio, F., Maraschi, L., Sambruna, R. M., et al. 2004, *ApJ*, 614, 64
 Uchiyama, Y., Urry, C. M., Cheung, C. C., et al. 2006, *ApJ*, 648, 910
 Vanden Berk, D. E., Richards, G. T., Bauer, A., et al. 2001, *AJ*, 122, 549
 Vanden Berk, D. E., Wilhite, B. C., Kron, R. G., et al. 2004, *ApJ*, 601, 692
 Vignali, C., Brandt, W. N., Schneider, D. P., Garmire, G. P., & Kaspi, S. 2003, *AJ*, 125, 418
 Volonteri, M., Haardt, F., Ghisellini, G., & Della Ceca, R. 2011, *MNRAS*, 416, 216
 Wall, J. V., & Jenkins, C. R. 2012, *Practical Statistics for Astronomers*, Cambridge, UK: Cambridge University Press
 Wang, R., Wagg, J., Carilli, C. L., et al. 2011, *AJ*, 142, 101
 Weisskopf, M. C., Wu, K., Trimble, V., et al. 2007, *ApJ*, 657, 1026
 Wilkes, B. J., & Elvis, M. 1987, *ApJ*, 323, 243
 Worrall, D. M., Tananbaum, H., Giommi, P., & Zamorani, G. 1987, *ApJ*, 313, 596

Wright, E. L., Eisenhardt, P. R. M., Mainzer, A. K., et al. 2010, *AJ*, 140, 1868
 Wright, A. E., Griffith, M. R., Burke, B. F., & Ekers, R. D. 1994, *ApJS*, 91, 111
 Wu, J., Brandt, W. N., Miller, B. P., et al. 2013, *ApJ*, 763, 109 (Wu13)
 Wu, J., Ghisellini, G., Hodges-Klück, E., et al. 2017, *MNRAS*, 468, 109
 Yang, J., Wang, F., Wu, X.-B., et al. 2016, *ApJ*, 829, 33
 Yuan, W., Fabian, A. C., Celotti, A., & Jonker, P. G. 2003, *MNRAS*, 346, L7
 Zamfir, S., Sulentic, J. W., & Marziani, P. 2008, *MNRAS*, 387, 856

APPENDIX A: STATISTICAL TESTING FOR EXTENDED STRUCTURE

The *Chandra* Cycle 17 objects mostly have limited photon counts. It is not feasible to directly compare their images with the PSF images to check for extended X-ray jets (e.g. Wu et al. 2017). We first produced the PSF image for each observation using ray-tracing²⁶ with a large number of simulated events. The statistical method we used is as follows.

We only consider $D \times D$ patches of pixels centred at the source position on the X-ray image and PSF image. The net source counts (N_{src}) and background counts (N_{bkg}) of the X-ray image are estimated using photometry (see Section 3). We add background events to the PSF image with a total number of

$$N_{\text{bkg,psf}} = \frac{N_{\text{bkg}}}{N_{\text{src}}} N_{\text{src,psf}}, \quad (\text{A1})$$

where $N_{\text{src,psf}}$ is the total number of simulated events in the PSF image. We then “flatten” the 2-dimensional images to sequences of pixels of length $L = D \times D$. The distribution of events in the PSF image is multinomial, with the estimated probability of i -th pixel

$$p_i = \frac{n_{i,\text{psf}} + N_{\text{bkg,psf}}/L}{N_{\text{src,psf}} + N_{\text{bkg,psf}}}, \quad (\text{A2})$$

where $n_{i,\text{psf}}$ is the number of events in the i th pixel of the PSF image with $N_{\text{src,psf}} = \sum_i n_{i,\text{psf}}$.

The likelihood of observing the X-ray image of a point source given the PSF’s multinomial distribution is

$$P(\text{X-ray image}|\text{PSF}) = \frac{N_{\text{src}}!}{n_1!n_2!\dots n_L!} \prod_{i=0}^L p_i^{n_i}, \quad (\text{A3})$$

where n_i is the number of events in the i -th pixel of the observed X-ray image with $N_{\text{src}} = \sum_i n_i$. We define a simpler statistic

$$S = - \sum_{i=1}^L [n_i \ln p_i - \ln(n_i!)], \quad (\text{A4})$$

which is the negative log-likelihood, omitting constants. The calculation is reduced by realizing that n_i is mostly 0 or 1 in the case of low counts. By drawing a large set of samples

²⁶ <http://cxc.harvard.edu/cal/Hrma/SAOTrace.html> and <http://space.mit.edu/CXC/MARX/>

from the multinomial distribution (p_1, \dots, p_L) , we obtain the empirical distribution of S , from which the p -value can be calculated. See Fig. A1 (left) for the example of SDSS J0813+3508.

In our calculation, we used $D = 20$ (i.e. the size of the patch is $10'' \times 10''$). We found a detection for the 0.5–8 keV image of SDSS J0813 + 3508 with $p = 0.0108$, which becomes less significant (the p -value increases to $p = 0.0832$) after taking into account the number of tests we have performed (e.g. Conrad 2015). We then compared the radio and X-ray images of SDSS J0813 + 3508, and did not find extended X-ray structure that corresponds to the radio jet, as shown in Fig. A1 (centre and right). Note that the extended radio component that is $\approx 7''$ away from SDSS J0813 + 3508 has a peak radio flux density (11.9 mJy) that is about half that of the core (20.0 mJy). We estimated the (observed-frame 0.5–2 keV) surface brightness coincident with the extended radio component to be $< 1.43 \times 10^{-16}$ erg cm $^{-2}$ s $^{-1}$ arcsec $^{-2}$, which means that the extended jet (if it exists) must be more than 10 times dimmer than the core in X-rays. Other sources are consistent with point sources. We conclude that no statistically convincing extended structure is found in the X-ray images.

We investigated further the constraints coming from the non-detections on the relative brightness of X-ray jets. In the X-ray images, we put an artificial point source $2''$ (4 pixels; the typical size of the resolved X-ray jets for quasars at $z > 4$) away from the core and increase its intensity until it is detected with the statistical tests above. Typically 3–4 photons are needed for the artificial jets to be detected. Therefore, any X-ray jets have to be $\gtrsim 3$ –25 times fainter than the cores for the *Chandra* Cycle 17 quasars, consistent with previous X-ray upper limits for high- z RLQs (e.g. Bassett et al. 2004; Lopez et al. 2006).

APPENDIX B: THE EFFECTS OF NON-SIMULTANEOUS DATA AND MEASUREMENT ERRORS

Since both types of uncertainties under consideration, measurement errors and variability, are stochastic in nature, it is impossible to apply corrections to the observed data to obtain underlying “true” values. The purpose of the Monte Carlo simulation is to add more fluctuations to the data and observe the consequence of the enlarged uncertainties. We created degraded samples by adding random numbers drawn from $N(0, 0.06^2)$ (a Gaussian distribution with zero mean and standard deviation $\sigma = 0.06$) to the observed $\Delta\alpha_{\text{ox}}$ (only detections). The statistical significance typically drops by $\sim 1\sigma$ using these worsened values, which is expected because more noise will tend to wash out the differences between the two distributions.

To demonstrate further the effects of uncertainties, we performed Bayesian fitting using a Gaussian structural model. What we provide below is a largely simplified version of the model of Kelly (2007). We assume the uncertainties on $\Delta\alpha_{\text{ox}}$ due to measurement errors and variability are Gaussian distributed with standard deviation $\sigma_e = 0.06$. We assume $\Delta\alpha_{\text{ox}}$ follows a Gaussian distribution with mean μ (identical to the median) and standard deviation σ_i . Here, σ_i represents the part of the scatter of the $\alpha_{\text{ox}}-L_{2500\text{\AA}}$ and

$L_{2 \text{ keV}}-L_{2500 \text{\AA}}-L_{5 \text{ GHz}}$ relations that cannot be explained by measurement error and variability (e.g. Gibson et al. 2008). The structural model is formulated as

$$\mu \sim \text{Uniform}(-1, 1), \quad (\text{B1})$$

$$\sigma_i \sim \text{Uniform}(0, 1), \quad (\text{B2})$$

$$\Delta\alpha_{\text{ox}}^{\text{true}} \sim N(\mu, \sigma_i^2), \quad (\text{B3})$$

$$\Delta\alpha_{\text{ox}}^{\text{obs}} \sim N(\mu, \sigma_i^2 + \sigma_e^2). \quad (\text{B4})$$

Following Section 5.2 of Kelly (2007) and considering cases with both detections and non-detections, the likelihood of the model parameters is

$$\begin{aligned} \ln \mathcal{L} = & - \sum_{j=1}^{N_{\text{det}}} \frac{(\mu - \Delta\alpha_{\text{ox},j})^2}{2(\sigma_i^2 + \sigma_e^2)} - \frac{1}{2} N_{\text{det}} \ln[2\pi(\sigma_i^2 + \sigma_e^2)] \\ & + \sum_{k=1}^{N_{\text{non-det}}} \ln \left[\int_{-\infty}^{\Delta\alpha_{\text{ox},k}} N(\mu, \sigma_i^2 + \sigma_e^2) dx \right], \end{aligned} \quad (\text{B5})$$

where N_{det} and $N_{\text{non-det}}$ are the numbers of detections and non-detections, respectively. We have used $\Delta\alpha_{\text{ox},j}$ and $\Delta\alpha_{\text{ox},k}$ to denote the values of detections and assigned upper limits for non-detections, respectively. The above likelihood has taken the uncertainties into account by marginalising them out.

We have drawn samples from the posterior distributions of μ and σ_i for $\Delta\alpha_{\text{ox,RQQ}}$ and $\Delta\alpha_{\text{ox,RLQ}}$ for both redshift bins. We plot in Fig. B1 the comparison of μ for different redshift bins. The impact of the sample size reflects itself in the concentration of the distribution: the mean of the low- z sample is better constrained than that of the high- z sample. Student’s t -tests return, practically, $p = 0.0$, i.e. it is almost impossible for the centres of the $\Delta\alpha_{\text{ox}}$ distributions for the different redshift bins to be consistent with each other, after considering the smearing effect of uncertainties.

In addition to hypothesis testing, the modelling process above can also be used to calculate the amount of X-ray enhancement (Section 4.3). Fig. B1 (right) indicates that the $\Delta\alpha_{\text{ox,RLQ}}$ of HRLQs at $z > 4$ are larger than that of HRLQs at $z < 4$ by 0.13 ± 0.03 on average, which is consistent with the result of the Kaplan-Meier estimator.

APPENDIX C: KAPLAN-MEIER ESTIMATOR AND BOOTSTRAPPING

Some HRLQs in the Miller11 sample have only upper limits for their X-ray fluxes, which leads to the corresponding measurements of $\Delta\alpha_{\text{ox}}$ also being upper limits. Therefore, we measure the median of $\Delta\alpha_{\text{ox}}$ using the Kaplan-Meier curve (Kaplan & Meier 1958), which is a maximum-likelihood estimator of the survival function (or, equivalently, the cumulative distribution function). To justify its application to our problem, we briefly provide in the below a heuristic derivation of the Kaplan-Meier estimator based on the assumption that whether an HRLQ is detected or not in X-rays is independent of the true value of its $\Delta\alpha_{\text{ox}}$, which is essential for the application of survival analysis (e.g. Avni et al. 1980; Wall & Jenkins 2012). The upper limits of $\Delta\alpha_{\text{ox,RQQ}}$ and $\Delta\alpha_{\text{ox,RLQ}}$ from Miller11 spread across a wide dynamic range (see Fig. 7), and thus we think this assumption is reasonable. The derivation deals with left-censored data (data

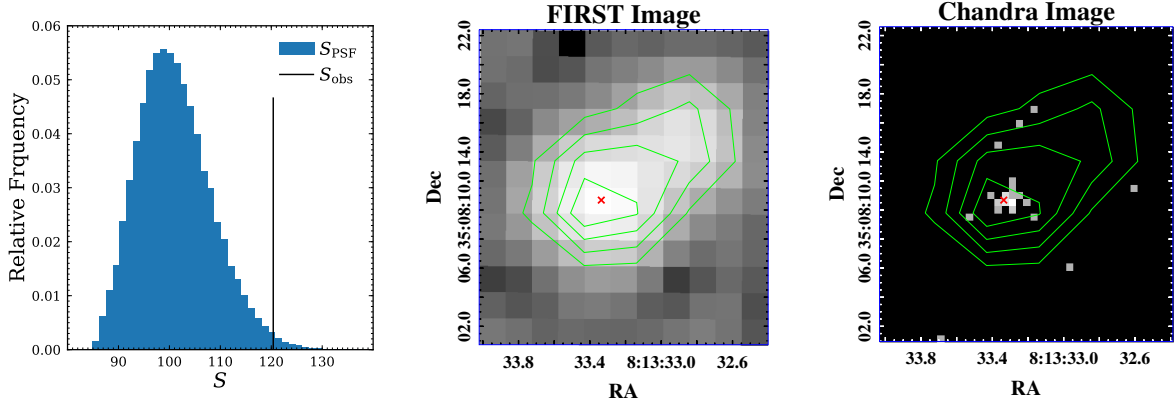


Figure A1. Left: The empirical distribution of S (blue histogram) calculated using simulated images of the *Chandra* PSF, together with the S value (vertical black line) calculated using the observed 0.5–8 keV *Chandra* image of SDSS J0813 + 3508. Centre: Radio image of SDSS J0813 + 3508 from FIRST at 1.4 GHz. Right: X-ray image of SDSS J0813 + 3508 in the 0.5–8 keV band. The red “x” symbols in both the centre and right panels indicate the optical position of the quasar. Contours of the radio image are plotted in both the centre and right panels, where the radio surface brightness increases from 2.9 mJy beam⁻¹ (outermost) to 12.2 mJy beam⁻¹ (innermost) with a step size of 3.3 mJy beam⁻¹. Even though S_{obs} appears marginally inconsistent with the distribution predicted by the *Chandra* PSF (left, $p \approx 0.011$), the X-ray image (right) does not show an extended structure that corresponds to the structure in the radio image (centre).

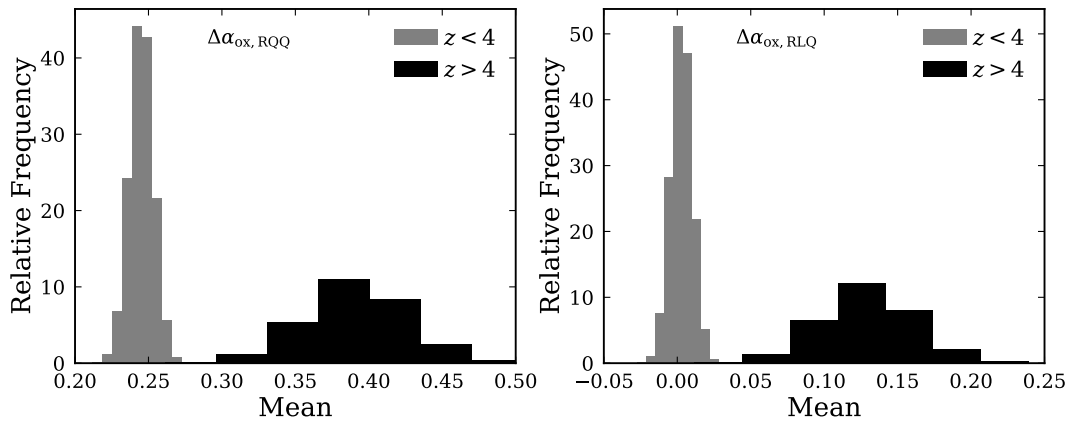


Figure B1. The posterior distribution of the means (also medians) of $\Delta\alpha_{\text{ox,RQQ}}$ (left) and $\Delta\alpha_{\text{ox,RLQ}}$ (right), where grey denotes the low- z sample and black denotes the high- z sample.

with upper limits) that are common in the astronomical context, while most of the statistical literature deals with right-censored data (data with lower limits).²⁷

We treat the result of each observation as a pair of the underlying value and the observational limit (X, X_{lim}); for the observations in the region of $X < X_{\text{lim}}$, only the upper limit is recorded. We plot a mock experiment in Fig. C1 (left), where detections are shown as stars in the bottom-right triangle on the plane, and upper limits are shown as leftward arrows on the diagonal. We define the cumulative distribution function $\Psi(x) \equiv P(X \leq x)$. The key observation of the left panel of Fig. C1 is that, under the assumption of the independence of X and X_{lim} ,

$$\frac{d\Psi}{\Psi(x)} = \frac{dD}{C(x)} \quad (\text{C1})$$

²⁷ Feigelson & Nelson (1985) circumvent this by providing a prescription that converts left-censored data to right-censored data.

follows, where $D(x)$ denotes the number of detections in a narrow strip at x , below the line of $X = X_{\text{lim}}$ (green-shaded region), and $C(x)$ denotes the number of observations (including detections and upper limits) in the rectangle left of x (yellow-shaded region). This is because the data points below the dashed purple line in Fig. C1 (left) form a subsample that has the same $\Psi(x)$ as that of the complete sample. The solution of $\Psi(x)$ is

$$\Psi(x) = A \exp \left[\int \frac{dD}{C} \right] = A \exp \left[\int_{-\infty}^x \frac{dx'}{C(x')} \frac{dD(x')}{dx'} \right] \quad (\text{C2})$$

$$= A \prod_{i: x_i \leq x} \frac{C^-(x_i) + D(x_i)}{C^-(x_i)} \quad (\text{C3})$$

where we explicitly differentiate the regions of C excluding D and including D , using C^- and C^+ , respectively. Note that i is only the index for detections. Therefore, the Kaplan-Meier estimator of the cumulative distribution function here is a series of increasing step functions, and the jumps only

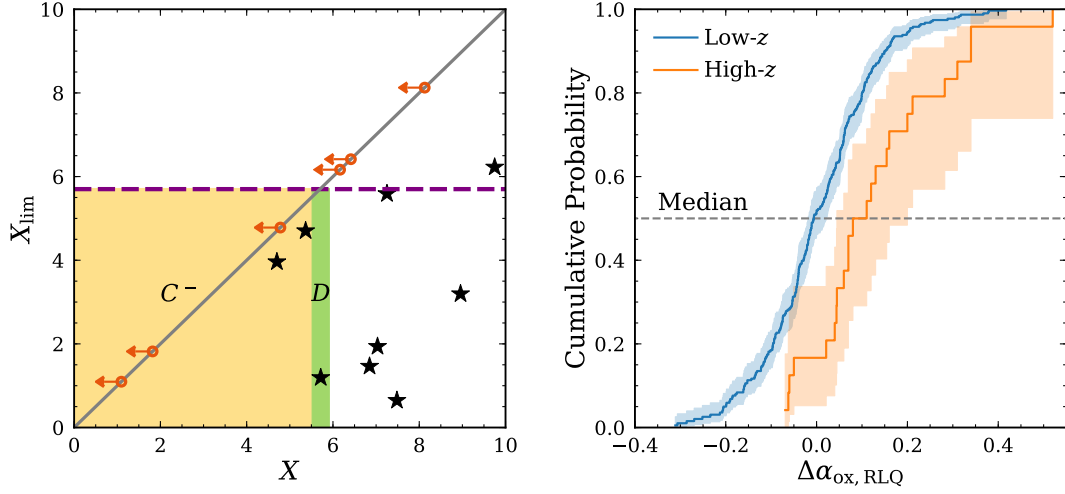


Figure C1. Left: The x -axis is the value of detection, and the y -axis is the limit of each observation. Upper limits are shown as leftward arrows, in contrast to detections that are shown as stars. The number of detections in the narrow green area is noted as D ; the number of observations (including detections and upper limits) in the non-overlapping yellow-shaded area is noted as C^- . A sub-sample is defined by the dashed purple line, under which the data points can represent the distribution of that of the complete sample on X direction if X and X_{lim} are independent of each other. Right: The cumulative probability distribution of $\Delta\alpha_{\text{ox,RLQ}}$ of the flux-limited samples of HRLQs at high redshift (orange) and low redshift (blue). The crossing points of the horizontal dashed lines with the curves are medians.

happen at the values of detections. The factor A can be chosen as

$$A = \prod_i \frac{C^-(x_i)}{C^-(x_i) + D(x_i)} \quad (\text{C4})$$

so that $\Psi(x) = 1$ at $x \geq x_{\text{max}}$. Therefore, the Kaplan-Meier estimator for the cumulative distribution function is

$$\Psi(x) = \prod_{i:x_i > x} \frac{C^-(x_i)}{C^-(x_i) + D(x_i)} = \prod_{i:x_i > x} \left[1 - \frac{D(x_i)}{C^+(x_i)} \right] \quad (\text{C5})$$

For most cases, each measured x_i is a discrete quantity, i.e. $D(x_i) = 1$. However, in the bootstrapping we performed below, we will also have $D(x_i) > 1$. We have used a Python package²⁸ to calculate the Kaplan-Meier estimator. We show an example of the cumulative distribution function in Fig. C1 (right), where the crossing points of the horizontal dashed line with the S-shaped curves are the median estimates. We calculate the difference of the medians to quantify the X-ray enhancement of HRLQs at $z > 4$ relative to HRLQs at low redshifts. We bootstrapped the samples of $\Delta\alpha_{\text{ox}}$ (1000 times) to estimate the dispersion of medians, as well as the scattering of the difference of medians.

This derivation is motivated by that of the C^- method in Lynden-Bell (1971), based on the similarity between their mathematical forms. The estimator of the survival function for right-censored data can be easily derived from a plot that is similar to Fig. C1 (left), where the detections are in the top-left triangle of the $X_{\text{lim}}-X$ plane and lower limits are rightward arrows on the diagonal. See Feigelson & Nelson (1985) and Schmitt (1985) for a complete discussion on astronomical applications of the Kaplan-Meier estimator and Avni et al. (1980) for a different algorithm that works with singly censored astronomical data.

This paper has been typeset from a $\text{\TeX}/\text{\LaTeX}$ file prepared by the author.

²⁸ <http://lifelines.readthedocs.io/en/latest/>